

COMPARATIVE ANALYSIS BETWEEN SYNCHRONOUS
GENERATORS AND VIRTUAL SYNCHRONOUS MACHINE
GRID-FORMING INVERTER

by

UEKAWA Vitor Eiti

A Master Thesis

Submitted to

the School of Engineering of Tokyo Institute of Technology

on February 3, 2024

for the Degree of Master of Science

in Systems and Control Engineering

ABSTRACT

Acknowledgements

Contents

1	Introduction	1
1.1	Background	1
1.2	Objectives	3
1.3	Structure of the Thesis	3
2	Overview of Main VSM Topologies	4
2.1	VSYNC Project's VSM Topology	4
2.2	IEPE's VSM Topology	5
2.3	KHIs' VSM Topology	8
2.4	ISE Lab's VSM Topology	9
2.5	Synchronverter	10
2.6	Cascaded Virtual Synchronous Machine	11
2.7	Summary of VSM Topologies	13
3	Mathematical Modeling of VSM	15
3.1	Overall System Topology and Control Scheme	15
3.2	Mathematical Modeling of VSC	16
3.2.1	PWM Modulation	17
3.2.2	Park's Transformation ($dq\theta$ -Transformation)	18
3.2.3	Averaged Model of VSC	19
3.3	Mathematical Modeling of VSM	21
3.4	Mathematical Modeling of Cascaded PI Controller	24
3.5	Calculation of Equilibrium Point	25
	Appendices	26
A	Synchronous Generators	27
A.1	Modeling of Synchronous Generators	27
A.1.1	General Structure of Synchronous Generators	27
A.1.2	Linear Magnetic Circuit	29
A.1.3	Park's Transformation ($dq\theta$ -transformation)	30
A.1.4	Per-Unit System	32
A.1.5	Park's Model (Detailed Model)	33
A.1.6	2-axis Model (Subtransient Model)	34
A.1.7	1-axis Model (Flux-Decay Model)	35
A.1.8	Classical Model	35
A.2	Modeling of Exciter and Automatic Voltage Regulator (AVR) . .	35
A.3	Modeling of Turbine/Governor	35
A.4	Power System Stabilizer (PSS)	35
A.5	Automatic Generation Control (AGC)	35

Chapter 1

Introduction

1.1 Background

The growing demand for energy and the challenges related to climate change require a transition towards renewable-based generation. Some examples of environmental requirements are discussed in the Sustainable Development Goals (SDGs) [1] and the Conference of the Parties (COP) [2] by the United Nations. It has been established that global net human-caused emissions of carbon dioxide (CO_2) need to decrease by approximately 45 percent from 2010 levels by 2030, reaching net zero around 2050.

As a consequence, the total share of energy generation from renewable sources has been increasing significantly in recent years. Some studies predict that by 2050, 91% of electricity generation will come from renewable resources, primarily solar and wind energy [3]. These emerging sources come in various sizes, ranging from residential-scale rooftop systems to utility-scale power plants, and they are interconnected across the electric grid, linking both the distribution system and the high-voltage transmission system. Significantly, for the focus of our study, a considerable number of these new resources connect to the power system through power electronic inverters[4].

Therefore, the transition towards renewable-based generation implies a shift from large centralized generation units, mainly composed of synchronous generators (SG), to decentralized/distributed generation units, mainly composed of inverter-based resources (IBR).

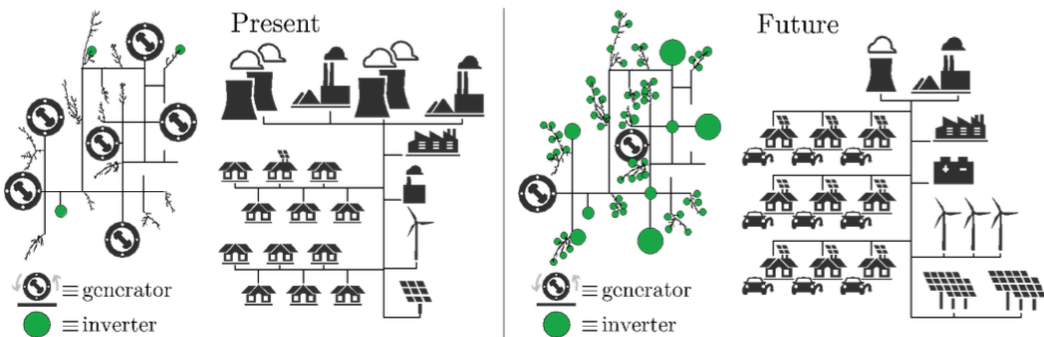


Figure 1.1: Present and future/projected power grids[4].

However, the replacement of SGs by IBRs has created new challenges for research related to stability requirements and the reliability and controllability of the system [5]. Some of the challenges include:

- Low inertia and frequency issues
- Fault Ride Through (FRT) capability issues
- Power quality issues
- Uncertainty issues

Among the several issues mentioned, the loss of system inertia is the most detrimental to the power system [5]. System inertia refers to the kinetic energy of all interconnected SGs of a power system [6]. In the case of a sudden increase in load or loss of generation, the kinetic energy stored in the SGs can bridge the gap between generation and consumption for a few seconds until a control action takes corrective measures. Since IBRs rely on electronic devices, they have very low or no inertia, and substituting SMs with IBRs would lead to a drastic reduction in the total system inertia.

In addition, today's IBRs generally rely on phase-locked loops (PLLs) to estimate the voltage angle at the inverter terminals, which is then used to control the inverter current output using vector control [7]. Therefore, these inverters "follow" the grid voltage and frequency, which are typically generated by SGs, and are called grid-following inverters (GFLI). Consequently, this control technique only works well in stiff AC grids with low frequency and voltage deviations.

In summary, the penetration of GFLI-based IBRs in power generation is very limited, as they have very low inertia and rely on a stiff AC grid. To address this problem, a new inverter control paradigm called grid-forming control has been developed. Grid-Forming Inverters (GFMI) act as ideal voltage sources actively controlling the magnitude of voltage and the frequency at the point of common coupling (PCC) [8].

Consequently, GFMI is expected to facilitate the development of scalable and decentralized AC power systems, wherein the voltages and frequency are controlled through the collaborative interactions among the grid-forming units. The subsequent figure elucidates the primary distinctions between GFMI and GFLI.

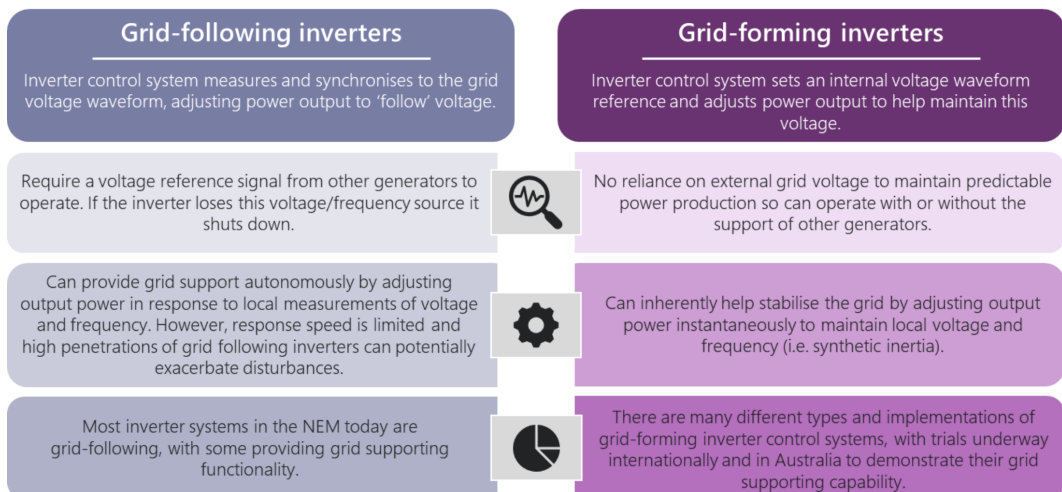


Figure 1.2: Differences between grid-following and grid-forming [9].

One of the most popular GFMI control approaches is based on introducing the SG dynamic models into the controllers of the inverter, enabling it to operate like a rotating electrical machine. This control approach is known as Virtual Synchronous Machine (VSM), and implementations of different orders have been reported in the literature, ranging from detailed electromechanical models [10][11] to simplified swing dynamics [12][13]. However, there is still little literature discussing the necessity of detailed electromechanical models, and models of intermediate complexity, such as the 1-axis (flux-decay) model, have not been reported yet [14].

1.2 Objectives

This thesis focuses on the modeling, simulation, and analysis of VSMs of different orders in a multi-machine power system with multiple SGs. The main goals of this project are to evaluate the necessity of detailed electromechanical models when implementing VSMs and to propose a VSM model equivalent to the 1-axis (flux-decay) SG model. The entire work is divided into the following steps:

1. Study of the modeling and simulation of voltage source power converters;
2. Study of the multiple implementations of VSMs;
3. Comparison between VSMs of multiple orders and 2-axis (subtransient) model of SG in terms of frequency deviation and output voltage and power under load increase and ground fault.

1.3 Structure of the Thesis

The remainder of this thesis is organized as follows. In Chapter 2, we present an overview of the main implementations of VSMs in the literature, from detailed electromechanical models to simplified swing dynamics. In Chapter 3, we present a detailed mathematical modeling of voltage source converters, and their controllers enabling the VSMs dynamics. Chapter 4 presents the. In the Appendix, we describe the modeling and simulation methods of main power system components such as SMs, loads and transmission lines.

Chapter 2

Overview of Main VSM Topologies

With the increasing penetration of Inverter-Based Resources (IBRs) and the diminished involvement of Synchronous Generators (SGs) in energy generation, existing power systems are experiencing a loss of inertia. This loss significantly impacts two key aspects. Firstly, the absence of kinetic energy in the system leads to a higher frequency nadir and a faster rate of change in frequency (RoCoF), thereby affecting power quality and potentially causing the tripping of generators [13].

One of the most promising solutions to address these challenges is the implementation of Virtual Synchronous Machines (VSMs). A VSM is a control technique applied to the switching patterns of voltage source converters (VSCs), aiming to replicate the dynamic behavior of SGs.

Among the most notable research groups working on VSMs are: the VSYNC project [15] under the 6th European Research Framework program, the Virtual Synchronous Machine (VISMA) project [10] at the Institute of Electrical Power Engineering (IEPE) of Clausthal University of Technology in Germany, the VSM research team at Kawasaki Heavy Industries (KHIs) [16], and the Laboratory for Power Electronics and Electrical Drives (formerly ISE Lab) at Osaka University [13, 17, 18]. In this chapter, we provide an overview and comparison of the topologies developed by these research groups.

2.1 VSYNC Project's VSM Topology

The VSYNC project, initiated under the 6th European Research Framework program, represents a pioneering effort in implementing virtual inertia control for inverters. This project's system comprised an energy storage unit, a DC link, and a power inverter with an output LCL filter connected to an AC electrical grid [15].

The control scheme incorporates a Phase-Locked Loop (PLL) and a current reference generation circuit. The PLL is used for synchronization with the grid frequency and for providing an angle reference for the dq transformation. Meanwhile, the current reference generation circuit generates the reference current for controlling the inverter's switching pattern through PWM modulation. The overall control scheme of the VSYNC topology is illustrated in the following image.

The current reference is calculated based on the reference active P^* and reactive Q^* powers, which are calculated according to the SG swing equation so

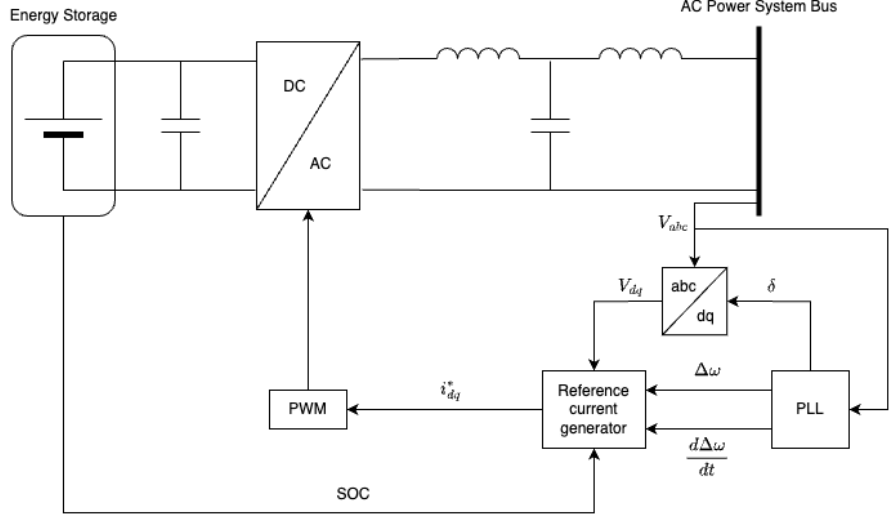


Figure 2.1: Overall control scheme of the VSYNC topology.

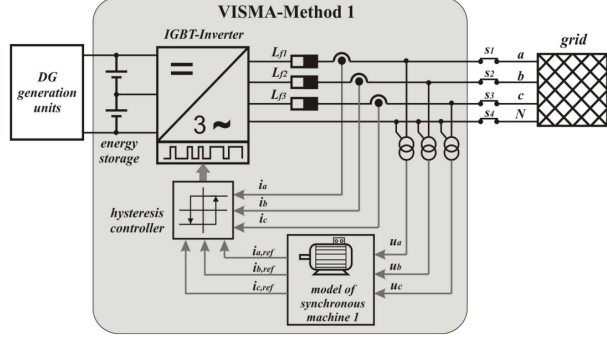
that the overall system can emulate the SGs inertial response.

$$\begin{aligned}
 P^* &= K_{SOC}\Delta SOC + K_P\Delta\omega + K_t \frac{\Delta\omega}{dt} \\
 Q^* &= K_V\Delta V \\
 i_d^* &= \frac{V_d P^* - V_q Q^*}{(V_d + V_q)^2} \\
 i_q^* &= \frac{V_d Q^* - V_q P^*}{(V_d + V_q)^2}
 \end{aligned}$$

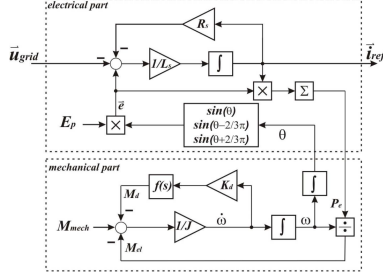
Overall, the VSYNC control scheme is a current-source based grid-supporting control mechanism, employing a current control loop at the output terminal and using a PLL to detect grid frequency and provide an angle reference for the dq transformation. It is important to note that the use of a PLL can negatively impact control performance under weak AC systems. Furthermore, the VSYNC control scheme incorporates only the SG swing equation.

2.2 IEPE's VSM Topology

The IEPE group has proposed a VSM topology named Virtual Synchronous Machine (VISMA), which initially utilized a current-source-based approach on a hysteresis controlled inverter [10, 19]. Subsequently, a voltage-source-based method was suggested to broaden its applicability to PWM controlled inverters, more prevalent in the market [20]. These are referred to as VISMA-Method 1 and VISMA-Method 2, respectively, with their control schemes depicted in subsequent figures.

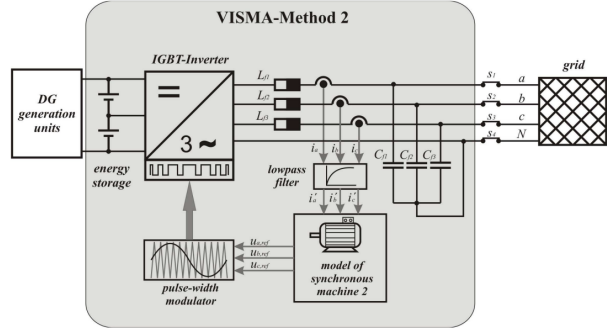


(a)

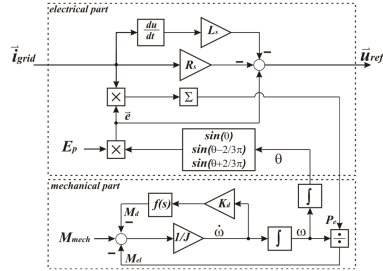


(b)

Figure 2.2: VISMA-Method 1 (current-source-based control) [20]. (a) Overall control scheme. (b) Model of synchronous machine 1.



(a)



(b)

Figure 2.3: VISMA-Method 2 (voltage-source-based control) [20]. (a) Overall control scheme. (b) Model of synchronous machine 2.

The VISMA-Method 1 consists in measuring the grid voltage to feed the virtual synchronous machine algorithm, which outputs a reference current analogous to the stator current of a SG. The virtual synchronous machine algorithm consists of an electrical part and a mechanical part that interact with each other. The mechanical part corresponds to the rotor dynamics of the virtual synchronous machine, and can be represented by the following equations:

$$\begin{aligned} M_{mech} - M_{el} &= \frac{1}{J} \frac{d\omega}{dt} + k_d f(s) \frac{d\omega}{dt} \\ M_{el} &= \frac{P_{el}}{\omega} \\ \theta &= \int \omega dt \end{aligned}$$

where J is the moment of inertia, k_d is the mechanical damping factor, $f(s)$ is the phase compensation term, ω is the angular speed, θ is the angular position and M_{el} and M_{mech} are the electrical and mechanical torque.

M_{mech} represents the action of the virtual governor, which is simplified as being a control input to the system. The excitation system is also simplified, being represented by an adjustable amplitude E_p , resulting in the following induced electromotive force in the virtual stator.

$$\vec{e} = E_p \begin{bmatrix} e_a \\ e_b \\ e_c \end{bmatrix} = E_p \begin{bmatrix} \sin(\theta) \\ \sin(\theta - \frac{2\pi}{3}) \\ \sin(\theta + \frac{2\pi}{3}) \end{bmatrix}$$

Then, this induced electromotive force is used with the measured grid voltage in the electrical part of the virtual synchronous machine model to calculate the reference current, which is then used to drive the hysteresis controlled converter. The electrical part of the synchronous machine model is represented by the following equations.

$$\begin{aligned} e_a - u_a &= i_a^{ref} R_s + L_s \frac{di_a^{ref}}{dt} \\ e_b - u_b &= i_b^{ref} R_s + L_s \frac{di_b^{ref}}{dt} \\ e_c - u_c &= i_c^{ref} R_s + L_s \frac{di_c^{ref}}{dt} \end{aligned}$$

where (u_a, u_b, u_c) are the measured grid voltage in each line, R_s and L_s are the virtual stator resistance and inductance, respectively.

The working principle of the VISMA-Method 2 is exactly the same as of the VISMA-Method 1, with the exception that the grid current is used instead of the grid voltage for calculating the reference signal to drive the PWM based converter. In other words, the electrical part of the synchronous machine model is now represented by:

$$e_a - u_a^{ref} = i_a R_s + L_s \frac{di_a}{dt}$$

$$e_b - u_b^{ref} = i_b R_s + L_s \frac{di_b}{dt}$$

$$e_c - u_c^{ref} = i_c R_s + L_s \frac{di_c}{dt}$$

where (i_a, i_b, i_c) are the measured grid current in each line.

It is important to highlight that the VISMA topology does not require a PLL and uses a 5th order model of a SG, comprising of two mechanical state variables (*theta* and ω) and 3 electromagnetic state variables (the stator quantities). However, the damper and excitation windings are not taken into consideration, and the transient and sub-transient dynamics are ignored. Moreover, this model does not consider possible saliency effects of the rotor.

Finally, it is important to highlight that the voltage-source-based VISMA control can be considered as an upgraded grid-forming control, and the current-source-based VISMA control can be considered as an upgraded grid-feeding control.

2.3 KHI's VSM Topology

KHI has proposed a current-source-based VSM topology in the *dq*-coordinate frame[16], which control diagram is illustrated in the following image.

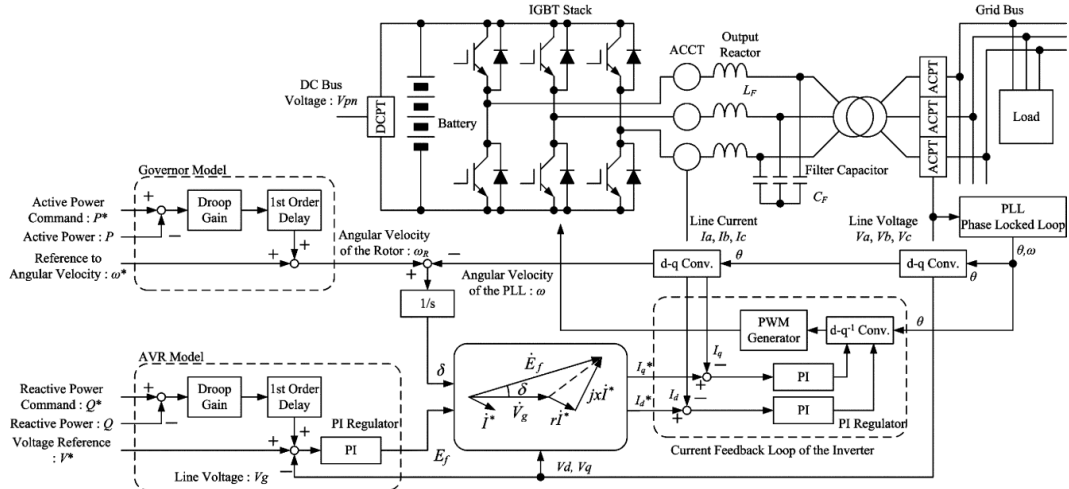


Figure 2.4: Control diagram of the VSM control developed by KHI[16].

In this model, the authors use phasor diagrams to express the relationship between the phase voltage and line currents of the virtual generator, thus ignoring the electrical dynamics. Moreover, the virtual generator is assumed to be cylindrical, with the same synchronous reactance on the direct and quadrature axes.

The model is composed of four main components: a PLL, an AVR, a virtual governor, a virtual generator model, and a current feedback loop. The PLL is used to detect the angular speed and angle of the grid side voltage of the inverter's output filter, which is used in the *dq*-transformations.

The output active and reactive powers are also measured, and they are in the virtual governor and AVR models to generate, respectively, the angular speed of the virtual rotor, and the internal electromotive force. The virtual governor and AVR models are simple PI controllers for active and reactive power regulation.

The outputs from the virtual governor and AVR are then used to compute the reference current, which then passes through a current feedback loop to generate the reference signal for the PWM modulation. Therefore, the VSM control by KHI is a current-source-based grid-supporting control.

2.4 ISE Lab's VSM Topology

The Laboratory for Power Electronics and Electrical Drives (formely ISE Lab) at Osaka University, which consists in emulating the SG swing equation [17, 21]. The following image describes the block diagram of the Ise Lab's VSM topology.

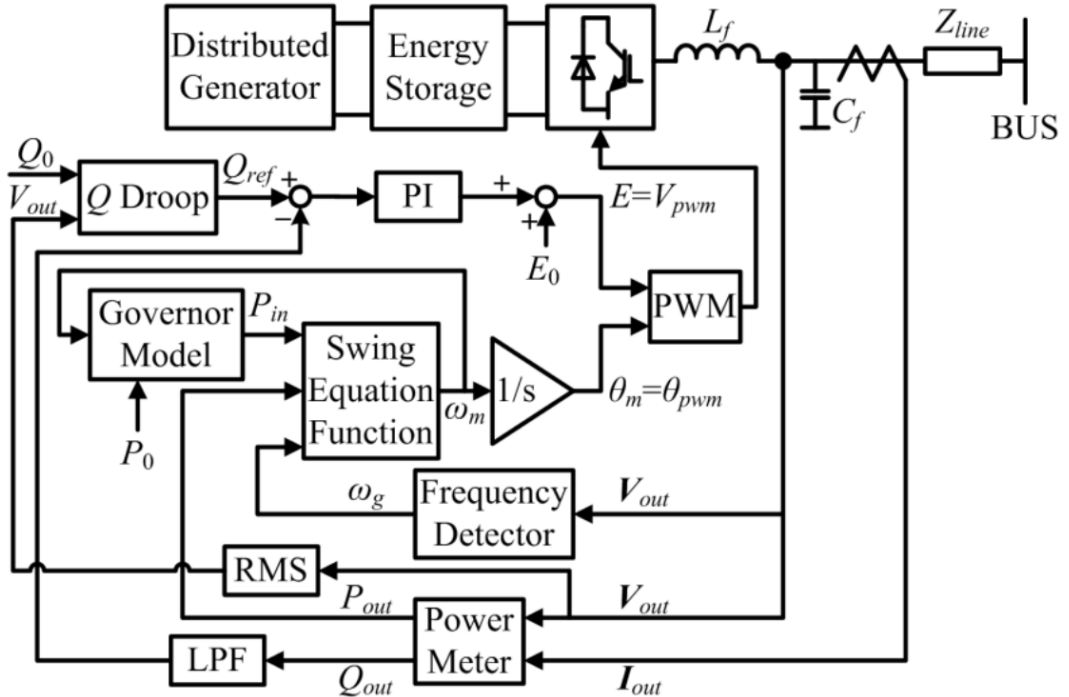


Figure 2.5: Control diagram of the VSM control developed by ISE Lab[22].

This model consists in measuring the output current and voltage, which are then used to compute the output active and reactive powers. The Frequency Detector block corresponds to a PLL that is used to measure the bus frequency ω_g which is used to compute the virtual rotor frequency through the swing equation:

$$P_{in} - P_{out} = J\omega_m \frac{d\omega_m}{dt} + D(\omega_m - \omega_g)$$

The rotor frequency is used as a reference for the governor model and the PWM inverter. Both the governor model and the Q Droop block are droop controllers creating linear droops between active power and frequency, and between reactive power and voltage, respectively.

It is important to highlight that no inner current or voltage loop is adopted in this control scheme, so that the filter reactance is analogous to the stator reactance of the VSM. Moreover, this VSM control can be classified as a voltage-source-based grid-supporting control.

2.5 Synchronconverter

Another well-known VSM topology is the Synchronconverter, which was proposed in 2009 by Qing-Chang Zhong and George Weiss. Initially, this topology was proposed for a three-phase inverter operated using PWM and LC filters to reduce the switching ripples [12]. The following figure illustrates the overall topology and control scheme for the Synchronconverter.

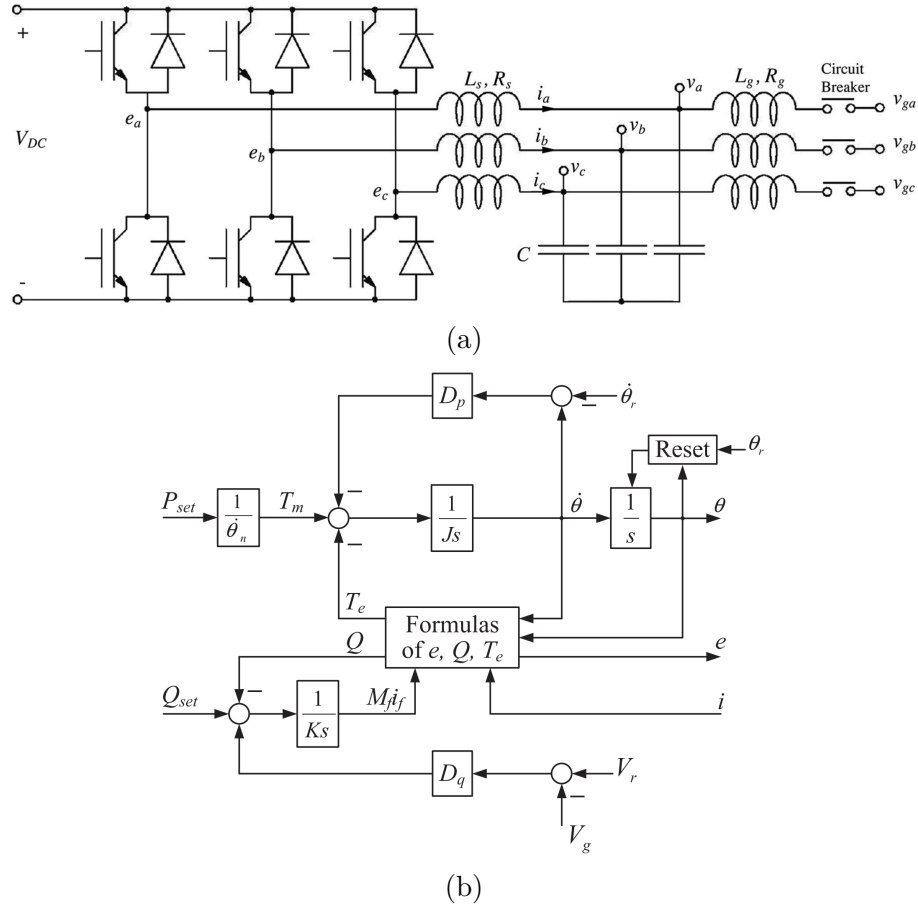


Figure 2.6: Synchronconverter (a) topology and (b) control scheme [23]

The modeling of the Synchronconverter is based on the simplification of the SG model by neglecting the damper windings in the rotor, and considering a round rotor. Therefore, only an exciter winding in the rotor, and the three windings in the stator are taken into consideration.

The system is designed based on the similarities between the dynamics of the output filter of the converter and the stator windings of a SG. In other words, so that the inverter's output filter dynamics match the dynamics of a SG. Therefore, L_s and R_s in Figure 2.6a are equivalent to the reactance and impedance of the

virtual generator, and the capacitor voltage (v_a, v_b, v_c) is equivalent to the stator terminal voltage. The relationship between terminal current $i = (i_a, i_b, i_c)$ and voltage $v = (v_a, v_b, v_c)$ is given by the following equation.

$$v = -R_s i - L_s \frac{di}{dt} + e$$

Therefore, the converter output voltage $e = (e_a, e_b, e_c)$ is controlled such that it follows the same dynamics of a SG's back electromotive force (EMF):

$$e = M_f i_f \dot{\theta} \begin{bmatrix} \sin(\theta) \\ \sin(\theta - \frac{2}{3}\pi) \\ \sin(\theta + \frac{2}{3}\pi) \end{bmatrix} - M_f \frac{di_f}{dt} \begin{bmatrix} \cos(\theta) \\ \cos(\theta - \frac{2}{3}\pi) \\ \cos(\theta + \frac{2}{3}\pi) \end{bmatrix}$$

where M_f is the mutual inductance between the virtual stator and rotor, i_f is the field excitation current, and θ is the virtual rotor angle is the virtual rotor angle. Here, i_f is used as an adjustable constant input, making the derivative term to become zero:

$$e = M_f i_f \dot{\theta} \begin{bmatrix} \sin(\theta) \\ \sin(\theta - \frac{2}{3}\pi) \\ \sin(\theta + \frac{2}{3}\pi) \end{bmatrix}$$

On the other hand, θ and $M_f i_f$ are calculated according to active and reactive power droop laws, respectively, as it can be seen in Figure 2.6b. The active P and reactive Q powers are calculated in the switching stage, corresponding to the multiplication between e and i .

Since the back EMF is used as a reference voltage for PWM modulation, the synchronverter is a voltage-source-based grid-supporting control method, and due to the lack of current control gives rise to a potential issue related to excessive high inrush fault current[24].

2.6 Cascaded Virtual Synchronous Machine

In 2013, a new VSM implementation approach was proposed by Salvatore D'Arco, Jon Are Suul and Olav B. Fosso[25, 26, 27]. In this thesis we call this implementation as Cascaded Virtual Synchronous Machine (CVSM), due to the fact that it includes two cascaded PI controls for voltage and current regulation. It is a voltage-source-based grid-supporting control method, and an overview of the system configuration and control scheme is illustrated in the Figure 2.7.

The system is modeled in the dq -frame, and the synchronization is realized by the power balance of the VSM swing equation. In other words, the coordinate transformations use the internal angle ω_{VSM} corresponding to the angle position of the virtual rotor. The presence of a PLL therefore does not introduce any instability problem.

The Virtual Inertia and Power Control block corresponds to the swing equation emulation, with the damping power/torque being proportional to the difference between the virtual rotor frequency and the grid frequency, thus the need of a PLL for estimation of the grid frequency. It is important to highlight that the damping power/torque is defined slightly differently from traditional

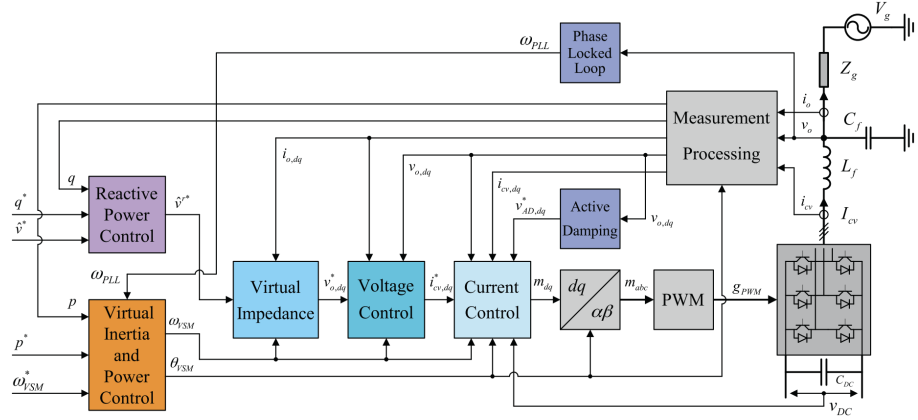


Figure 2.7: CVSM system topology and control scheme[27].

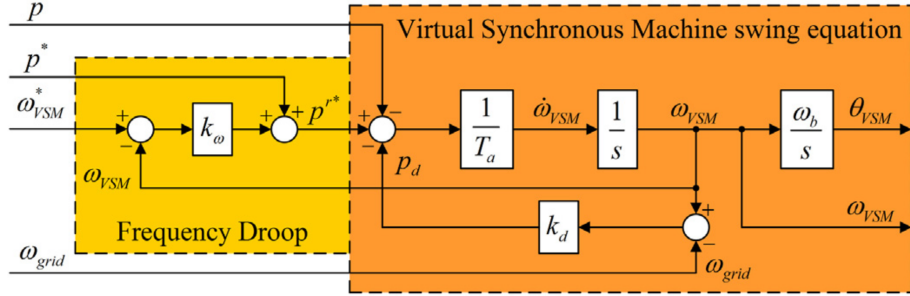


Figure 2.8: Control scheme of the Virtual Inertia and Power Control block[27].

SG modeling theory [28, 29]. Figure 2.8 illustrates the control scheme of the Virtual Inertia and Power Control block.

On the other hand, the reactive power control is implemented in a similar manner as the other VSM implementations, consisting in a droop law for the reactive power. The resulting signal is the voltage amplitude reference \hat{v}^r* , which is passed through a virtual impedance before it is used as a reference for the PWM modulation. This virtual impedance is analogous to the SG stator impedance and it is used for reducing the sensitivity of the VSM to small disturbances.

Finally, the resulting voltage reference vector v_0* is passed through a cascaded PI controller with feedforward terms to provide decoupling of the dq terms and allow for current and voltage limitation. Moreover, an additional voltage reference voltage magnitude corresponding to an active damping technique is added to the output of the PI current controller before being used for PWM modulation. The active damping is used for suppressing oscillations in the LC filter. The overall cascaded PI controller is illustrated in the Figure 2.9.

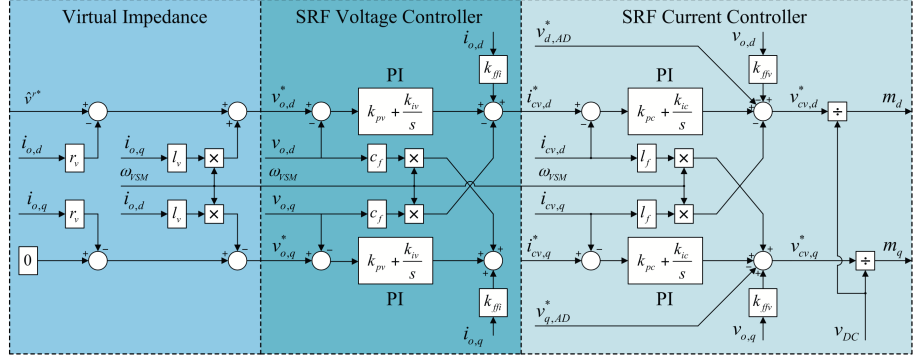


Figure 2.9: Virtual impedance and cascaded PI voltage control block scheme[27].

2.7 Summary of VSM Topologies

The following table summarizes the VSM topologies discussed in this Chapter according to characteristics that can be compared with SGs, such as control method, consideration of virtual damper windings, virtual impedance, need for PLL and overcurrent protection.

Topology	Control method	Virtual damper windings	Has virtual impedance?	Need PLL?	Has overcurrent protection?
VSYNC	current-source-based	0	No	Yes	Yes
VISMA-Method 1	current-source-based	0	Yes	No	No
VISMA-Method 2	voltage-source-based	0	Yes	No	No
KHI	current-source-based	0	Yes	Yes	Yes
ISE	voltage-source-based	0	No	Yes	No
Synchronverter	voltage-source-based	0	No	No	Yes
CVSM	voltage-source-based	0	Yes	Yes	Yes

Table 2.1: Summary of VSM topologies.

As established in Chapter 1, current-source-based grid-supporting control methods lack the capability to provide voltage support in weak grids with a high presence of Inverter-Based Resources (IBRs). Consequently, this thesis will not consider current-source-based grid-support control topologies.

Virtual impedance emulates the synchronous impedance behavior of traditional SGs and is instrumental in shaping system dynamics. Employing a PLL can adversely affect control performance in weak AC systems; therefore, PLL-free topologies are preferable. Furthermore, considering the susceptibility of power converters to high current levels, overcurrent protection is a critical safety feature.

According to Table 2.1, the CVSM topology meets all the stated requirements. Although it typically requires a PLL, it is implemented not for synchronization, and some authors have implemented this topology without the use of PLL [30]. Notably, this topology does not inherently include virtual damper windings.

As discussed in Chapter 1, damper windings in SGs are essential for damping oscillations and suppressing hunting, enhancing system stability [29, 28]. The primary distinction between low-order SG models (like the classical and 1-axis models) and high-order models (such as the 2-axis and Park's models) lies in the inclusion of damper windings. This feature has been incorporated into the CVSM topology in recent studies [31, 11].

This thesis will adopt the CVSM topology with the integration of virtual damper windings, following the approach used by [31, 11]. This will facilitate

a comprehensive comparison of the dynamic characteristics between SGs and VSMs of varying orders and assess the significance of including virtual damper windings.

Chapter 3

Mathematical Modeling of VSM

Chapter 2 described various VSM topologies available in the literature. Based on a comparison with SGs, we concluded the CVSM is the most suitable for operation in weak grids, since it provides voltage and frequency support, and has good stability since it is PLL free and has virtual impedance.

In this Chapter, we provide a detailed mathematical modeling of the CVSM topology, with some modifications to include the dynamics of the excitation and damper windings. In other words, we will aim to model the CVSM as SGs of different orders, such as the classical, the 1-axis and 2-axis models. First, a brief overview of the system topology and control scheme is illustrated. Then, the mathematical modeling of each physical and digital component is presented. Finally, we calculate the equilibrium point of the entire system for conducting numerical simulations in the next Chapter.

3.1 Overall System Topology and Control Scheme

This Section presents an overview of the system topology and control scheme, as depicted in Figure 3.1. For simplifying the representation, just a single phase of the circuit is represented in this image. The DC/AC inverter is assumed to be a two-level three-phase VSC, with each switch cell composed of a fully controllable, unidirectional switch in antiparallel connection with a diode. A DC source (battery, solar panel or other renewable resource) and a DC-Link are connected to the DC side of the inverter, whereas a LCL filter is connected to its AC side before connecting to the bus bar of a AC power grid. Since this thesis focuses on the control strategy of the grid-side, the dynamics of the DC source will be ignored, and the DC-link will be considered as a ideal constant voltage source.

As illustrated in Figure 3.1, the proposed VSG system is identical to the CVSM control scheme described in Section 2.6, except for some small modifications. First, the Virtual Inertia and Power Control, Reactive Power Control and Virtual Impedance blocks of Figure 2.7 are grouped in the SG Model block. In other words, we will represent and implement the active and reactive power regulation in the same manner as SGs, including not only the swing equation, but also the excitation and damping windings dynamics. Moreover, as it will be explained in Section 3.3, the damping power will be calculated based on the difference between the virtual rotor speed and the synchronous speed [32, 29, 28]. Thus, there is no need for a PLL.

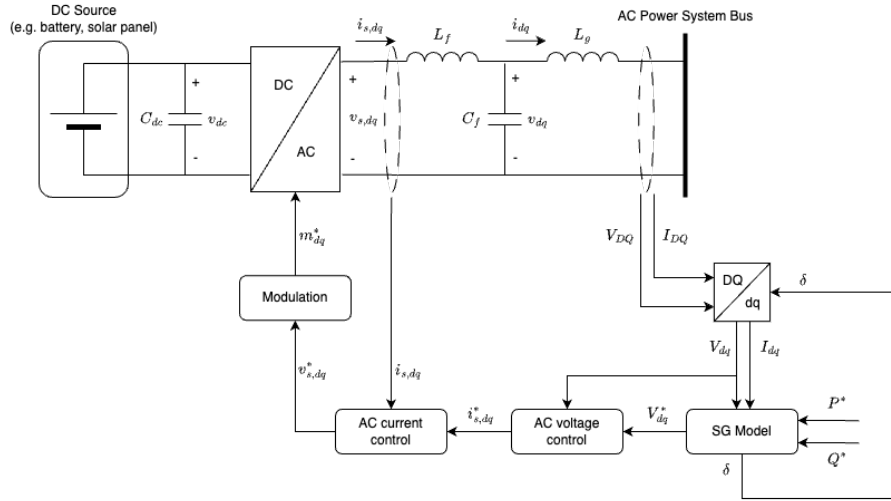


Figure 3.1: Overview of the system topology and control scheme.

In addition, since the objective of this thesis is to evaluate the importance of including the damper winding dynamics, every other damping technique, such as the Active Damping of the original CVSM in Section 2.6, will not be implemented. Finally, as it is will be explained in Section 3.2, in multimachine power system simulations, it is common to express all machines' variables into the Synchronously Rotating Reference Frame, converting balanced three-phase sinusoidal variations into constants. Thus, instead of employing $abc - dq0$ transformation, we use here the $DQ - dq$ transformation.

3.2 Mathematical Modeling of VSC

In this Section, we describe the assumptions and equations used to model the VSC illustrated in Figure 3.1. The inverter is assumed to be an ideal two-level three-phase VSC, with each cell being composed of a fully controllable, unidirectional switch in antiparallel connection with a diode, as illustrated in Figure 3.2.

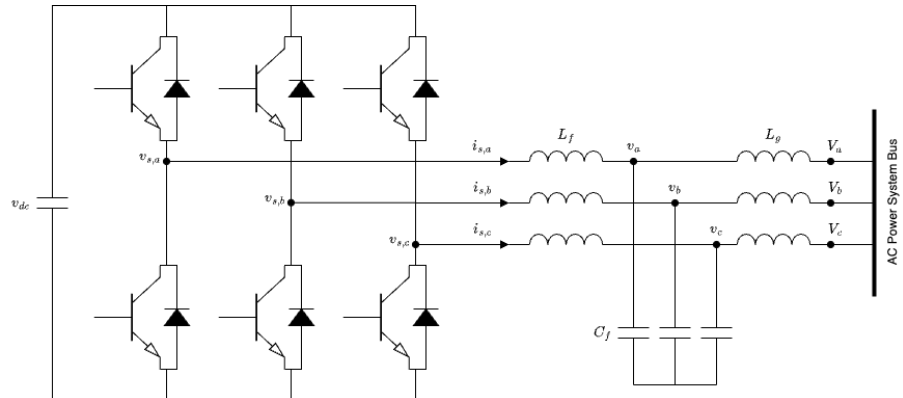


Figure 3.2: Overview of the system topology and control scheme.

The assumption of an ideal VSC implies in the following [33]:

- Each transistor or diode acts as a short circuit in its conduction state.

- Each transistor or diode switch acts as an open circuit in its blocking state.
- The transistors have no turn-off tailing current.
- The diodes have no turn-off reverse recovery current.
- Transitions from a conduction state to a blocking state, and vice versa, take place instantly.
- The AC-side current is a ripple-free DC quantity.

Moreover, we employ the averaged-model of the VSC, meaning that the dynamics of the average values will be analyzed, rather than analyzing the instantaneous values. By doing so, it is possible to describe the converter dynamics in function of the modulation signal, which is the main control variable. In the next subsections, we will present some fundamental theory for developing the averaged-model of the VSC.

3.2.1 PWM Modulation

The two-level three-phase VSC of Figure 3.2 is composed of three half-bridge converter connected in parallel to a common DC-side voltage source.

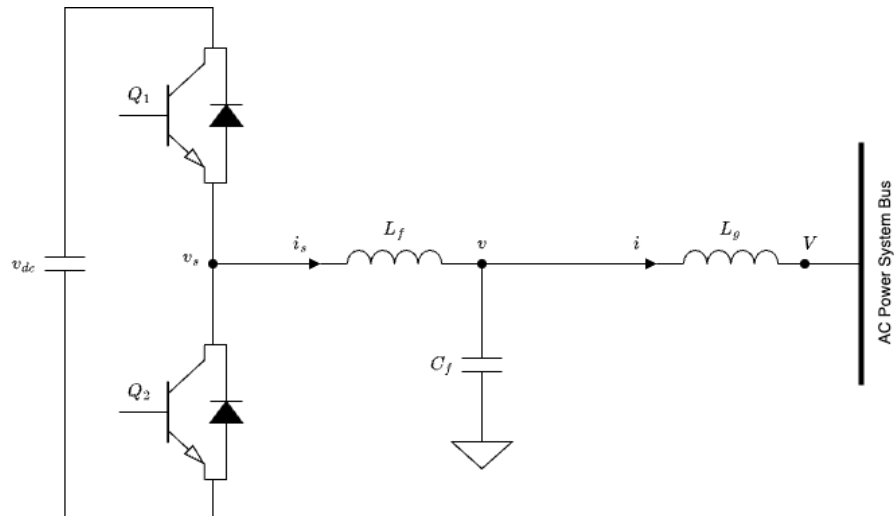


Figure 3.3: Half-bridge converter.

The operation of this converter consists in alternating the switches Q_1 and Q_4 , illustrated in Figure 3.3, which have different polarities. The turn-on/off commands of these switches can be implemented under various strategies, but the Pulse-Width Modulation (PWM) is the most popular technique used in inverters. This technique consists in comparing a periodic triangular waveform, the carrier signal, with the modulating signal, which is the desired output signal. The carrier signal has a periodic waveform with period T_s and varies between -1 and 1, and the switching of Q_1 and Q_4 is determined by the intersections between the carrier and modulating waveforms [33].

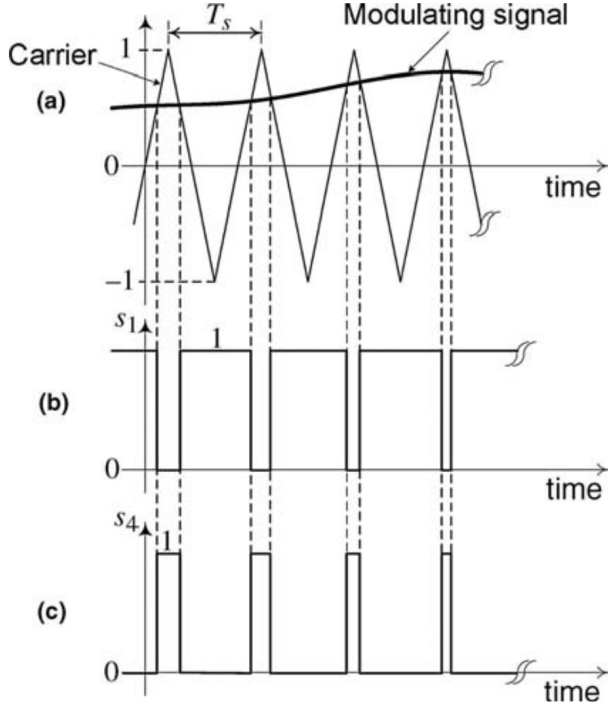


Figure 3.4: PWM switching strategy: (a) carrier and modulating waveforms, (b) switching function of switch Q_1 and (c) switching function of switch Q_4 [33].

From Figure 3.4, we notice that the half-bridge converter can be characterized by the following equations when controlled by PWM.

$$\begin{aligned} s_1 + s_4 &\equiv 1 \\ v_s &= \frac{v_{dc}}{2}s_1(t) - \frac{v_{dc}}{2}s_4(t) \end{aligned} \quad (3.1)$$

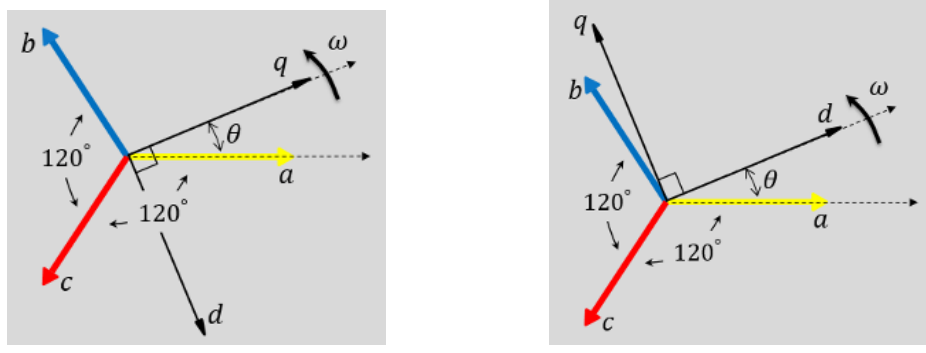
where s_1 and s_4 are the switching signals for Q_1 and Q_4 , respectively, v_{dc} is the voltage provided by the DC source and v_s is the voltage in the switching stage of the converter, as illustrated in Figure 3.3.

3.2.2 Park's Transformation (*dq0*-Transformation)

In power systems, the *dq0*-transformation, also known as Park's transformation, consists in converting from the static *abc* frame to a rotating *dq0* frame. The main objective of this transformation is to reduce a three-phase sinusoidal components into two-dimensional DC components, and therefore it results in relatively simple dynamic models that can be controlled through classical PID controllers.

This transformation slightly differs from author to author depending on the choice of the leading and lagging components. For instance, in [28] the authors consider the *a*-axis and the *q*-axis initially aligned, while in [32] the authors consider the *a*-axis and the *d*-axis initially aligned.

In this thesis, the *a*-axis and the *q*-axis are chosen to be initially aligned. In this case, the Park transformation can be expressed by the following transformation matrix from *abc* frame to the rotating *dq0* frame.



(a) The a -axis and the q -axis are initially aligned.
(b) The a -axis and the d -axis are initially aligned.

Figure 3.5: Different representations of $dq\theta$ frame.

$$T_{dq0} = \frac{2}{3} \begin{bmatrix} \sin(\omega t) & \sin(\omega t - \frac{2\pi}{3}) & \sin(\omega t + \frac{2\pi}{3}) \\ \cos(\omega t) & \cos(\omega t - \frac{2\pi}{3}) & \cos(\omega t + \frac{2\pi}{3}) \\ \frac{1}{2} & \frac{1}{2} & \frac{1}{2} \end{bmatrix} \quad (3.2)$$

where ωt is the angle of the q -axis with respect to the a -axis at time t . The inverse transformation can be expressed by the following matrix.

$$T_{dq0}^{-1} = \begin{bmatrix} \sin(\omega t) & \cos(\omega t) & 1 \\ \sin(\omega t - \frac{2\pi}{3}) & \cos(\omega t - \frac{2\pi}{3}) & 1 \\ \sin(\omega t + \frac{2\pi}{3}) & \cos(\omega t + \frac{2\pi}{3}) & 1 \end{bmatrix} \quad (3.3)$$

3.2.3 Averaged Model of VSC

Applying the Kirchhoff's current and voltage laws to the circuit in Figure 3.2, the following relationship between voltage and currents can be obtained.

$$\begin{cases} L_f \frac{di_{s,abc}}{dt} = v_{s,abc} - v_{abc} \\ C_f \frac{dv_{abc}}{dt} = i_{s,abc} - i_{abc} \\ L_g \frac{di_{abc}}{dt} = v_{abc} - V_{abc} \end{cases} \quad (3.4)$$

where $i_{s,abc} = [i_{s,a} \ i_{s,b} \ i_{s,c}]^\top$ is the vector of currents at the switching stage of the converter, $v_{abc} = [v_a \ v_b \ v_c]^\top$ is the vector of voltages across the filter capacitors, $i_{abc} = [i_a \ i_b \ i_c]^\top$ is the vector of output currents of the LCL filter and $V_{abc} = [V_a \ V_b \ V_c]^\top$ is the vector of output voltages of the LCL filter. Moreover, L_f , C_f and L_g are the filter inductances and capacitance.

From the theory of nonlinear systems, it is possible to average a signal by applying the following operator [33]:

$$\bar{x}(t) = \frac{1}{T_s} \int_{t-T_s}^{T_s} x(\tau) d\tau$$

where $x(t)$ denotes any physical quantity, and the overbar denotes its average. Thus, by integrating both sides of the first equation in Equation 3.4 for a single-phase:

$$\begin{aligned} \frac{1}{T_s} \int_0^{T_s} \left(L_f \frac{di_s(\tau)}{dt} \right) d\tau &= \frac{1}{T_s} \int_0^{T_s} (v_s(\tau) - v(\tau)) d\tau \\ L_f \frac{d}{dt} \left(\frac{1}{T_s} \int_0^{T_s} i_s(\tau) d\tau \right) &= \frac{1}{T_s} \int_0^{T_s} v_s(\tau) d\tau - \frac{1}{T_s} \int_0^{T_s} v(\tau) d\tau \\ L_f \frac{d\bar{i}_s}{dt} &= \frac{1}{T_s} \int_0^{T_s} v_s(\tau) d\tau - \bar{v} \end{aligned}$$

From Equation 3.1:

$$L_f \frac{d\bar{i}_s}{dt} = \frac{1}{T_s} \int_0^{T_s} \left(\frac{v_{dc}}{2} s_1(\tau) - \frac{v_{dc}}{2} s_4(\tau) \right) d\tau - \bar{v}$$

Moreover, since $s_1 + s_4 \equiv 1$ over the period T_s , let d denote the duty cycle of the inverter, then if $s_1 = 1$ over dT_s seconds, then $s_4 = 1$ must hold for $(T_s - dT_s)$ seconds, as illustrated in Figure 3.4. Therefore, the above equation becomes:

$$L_f \frac{d\bar{i}_s}{dt} = \frac{v_{dc}}{2} (2d - 1) - \bar{v}$$

Or, replacing $m = 2d - 1$, where m is the modulation amplitude, and considering the three-phases of the system:

$$L_f \frac{d\bar{i}_{s,abc}}{dt} = m_{abc} \frac{v_{dc}}{2} - \bar{v}_{abc}$$

where m_{abc} is a vector of the modulation amplitudes for each phase.

Repeating the same procedure to the remaining equations of Equation 3.4, the averaged model of the VSC can be described by:

$$\begin{cases} L_f \frac{d\bar{i}_{s,abc}}{dt} = m_{abc} \frac{v_{dc}}{2} - \bar{v}_{abc} \\ C_f \frac{d\bar{v}_{abc}}{dt} = \bar{i}_{s,abc} - \bar{i}_{abc} \\ L_g \frac{d\bar{i}_{abc}}{dt} = \bar{v}_{abc} - \bar{V}_{abc} \end{cases} \quad (3.5)$$

Moreover, multiplying both side of the equations by the transformation matrix A.6, we obtain the averaged model in the $dq0$ -frame.

$$\begin{cases} L_f \frac{di_{s,dq}}{dt} = -\omega L_f \mathcal{J}_2 i_{s,dq} + m_{dq} \frac{v_{dc}}{2} - v_{dq} \\ C_f \frac{dv_{dq}}{dt} = -\omega C_f \mathcal{J}_2 v_{dq} + i_{s,dq} - i_{dq} \\ L_g \frac{di_{dq}}{dt} = -\omega L_g \mathcal{J}_2 i_{dq} + v_{dq} - V_{dq} \end{cases} \quad (3.6)$$

where the dq subscripts indicate vectors of two dimensions, one corresponding to the d -axis component, and the another to the q -axis component. The entire system is considered symmetrical and balanced, thus the 0 component is ignored.

Moreover, $\mathcal{J}_2 = \begin{bmatrix} 0 & -1 \\ 1 & 0 \end{bmatrix}$ and the overbar indicating average value is removed for simplifying the notation.

3.3 Mathematical Modeling of VSM

The SG Model illustrated in Figure 3.1 corresponds to the outer loop of the system, and is responsible for active and reactive power regulation. In the topologies presented in Chapter 2 the active and reactive power regulation is implemented through the emulation of the swing equation and a $Q - V$ droop control, respectively.

In this thesis, the SG Model block will be implemented using the equations of SG models of different orders, namely the 2-axis, 1-axis and classical models. A similar implementation can be found in [34, 31] for the 2-axis model, and the implementation of the classical model is equivalent to that of the original CSVM implementation [27]. However, the implementation of the 1-axis model is not yet reported in the literature.

The SG Model block is composed of three main subsystems, one for emulating the swing equation, one for emulating the electromagnetic equations, and one corresponding to an automatic voltage regulator (AVR).

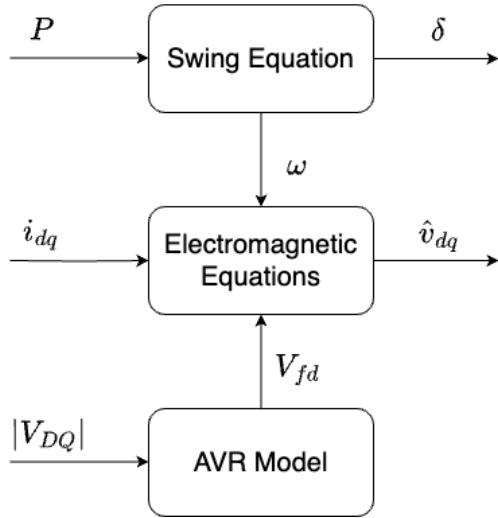


Figure 3.6: Subsystem of the SG Model block.

The digital implementation of the Swing Equation is illustrated by the schema block in Figure 3.7 where D is the damping coefficient, M is the inertia coefficient, $\Delta\omega = \omega - \omega_s$ corresponds to the frequency deviation from the synchronous speed, P^* is the active power setpoint, P is the converter output active power and δ is the virtual rotor angular position with respect to the synchronously rotating frame.

Moreover, the AVR Model is implemented according to Figure 3.8, where V^* is the output voltage setpoint, provided from the power flow calculation, $|V_{DQ}|$ is the converter output voltage magnitude, T_A is the amplifier time constant, K_A is the amplifier gain, V_R is the exciter input, T_F and K_F are the stabilizing transformer time constant and gain, respectively, R_f is the rate feedback, T_E , K_E and S_E are the exciter time constant, gain and saturation function, respectively.

The Swing Equation and AVR Model are the same for all SG implementations. It is important to note that usually the active power setpoint P^* is provided to the generator by its governor. However, in this thesis P^* will be considered constant and equal to the active power resulting from the power flow

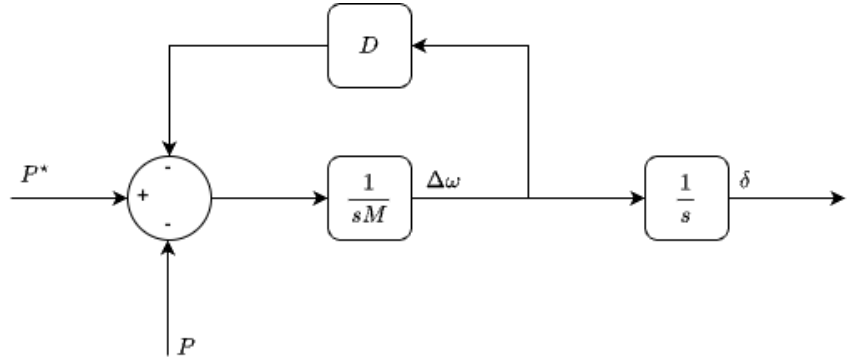


Figure 3.7: Schema block of the swing equation.

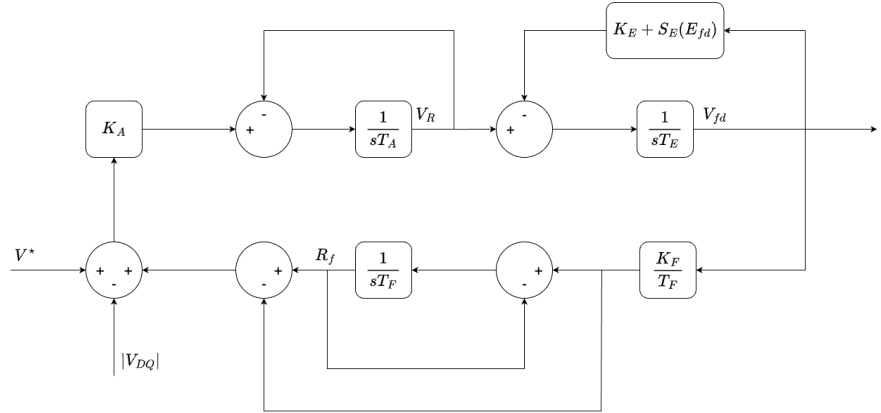


Figure 3.8: Schema block of the AVR.

calculation. This approximation results from the fact that the dynamics of the governor are normally much slower than that of the exciter [35].

On the other hand, the electromagnetic equations for the 2-axis, 1-axis and classical model are different, according to the number of damper windings taken into consideration. Please refer to [28] and to the Appendix A for more details about modeling of SGs. The schema blocks for the electromagnetic equations of each model are illustrated in Figures 3.11, 3.10 and 3.9.

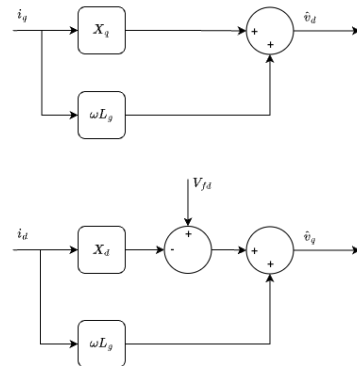


Figure 3.9: Schema block of electromagnetic equations of the classical model.

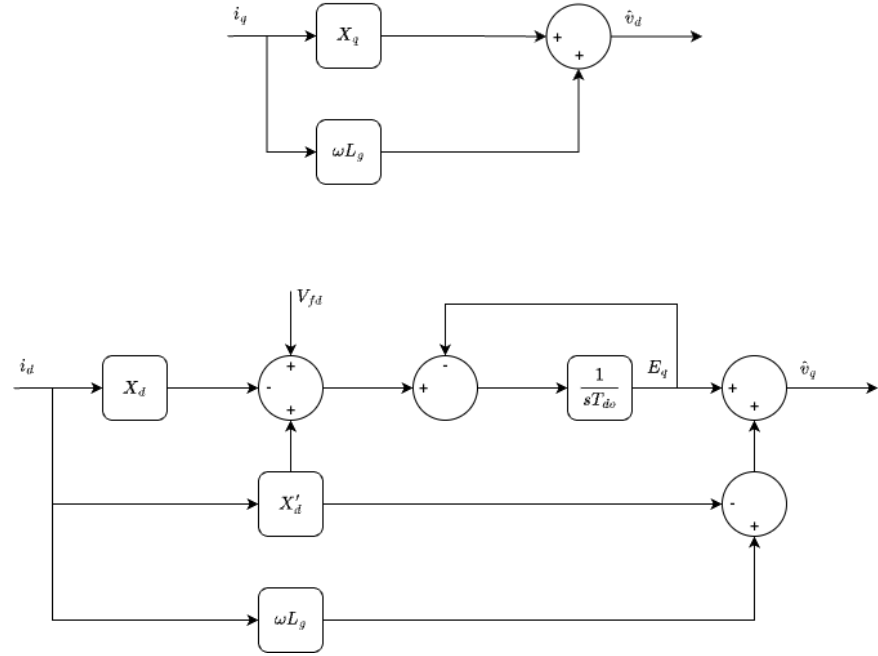


Figure 3.10: Schema block of electromagnetic equations of the 1-axis model.

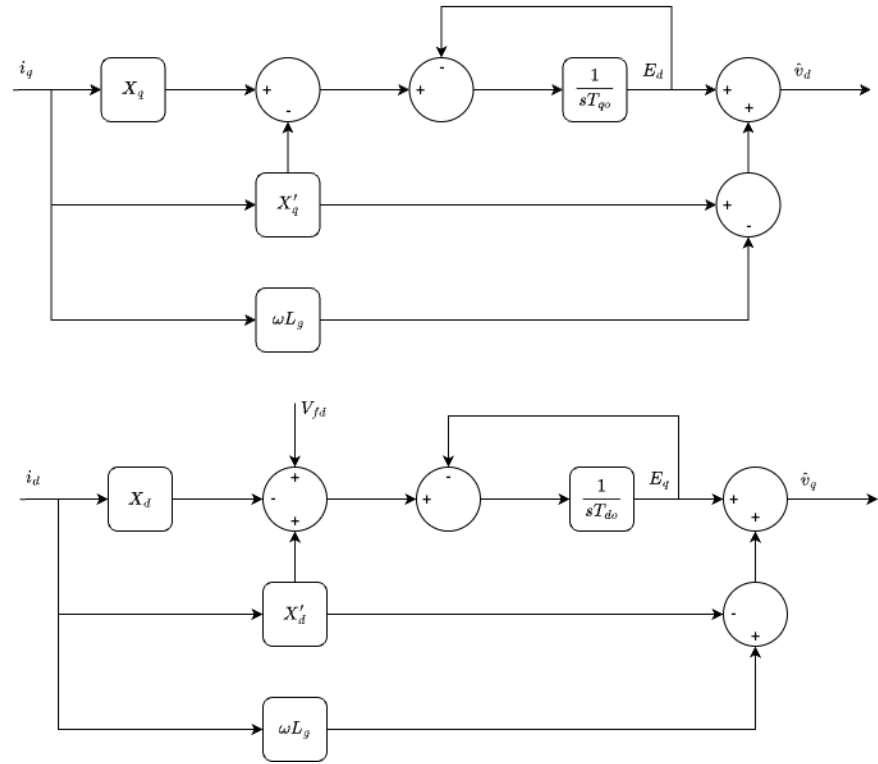


Figure 3.11: Schema block of electromagnetic equations of the 2-axis model.

In Figures 3.11, 3.10 and 3.9, X_d and X_q are the transient reactances, X'_d and X'_q are the subtransient reactances, T_{do} and T_{qo} are the windings time constants, E_d and E_q are the transient voltages and L_g is the converter LCL filter outer inductance. The feedforward terms $\omega L_g i_d$ and $\omega L_g i_d'$ are added to compensate the converter LCL filter outer inductance such that the filter output voltage

behaves similarly to a SG terminal voltage. The dynamic equations describing the SG Model block are:

2-axis SG

$$\begin{cases} \frac{d\delta}{dt} &= \omega_s \Delta\omega \\ M \frac{\Delta\omega}{dt} &= -D \Delta\omega + P^* - P \\ T'_{do} \frac{E_q}{dt} &= -E_q - (X_d - X'_d) I_d + V_{fd} \\ T'_{qo} \frac{E_d}{dt} &= -E_d + (X_q - X'_q) I_q \\ T_E \frac{dV_{fd}}{dt} &= -(K_E + S_E(V_{fd})) V_{fd} + V_R \\ T_F \frac{dR_f}{dt} &= -R_f + \frac{K_F}{T_F} V_{fd} \\ T_A \frac{dV_R}{dt} &= -V_R + K_A R_f - \frac{K_A K_F}{T_F} V_{fd} + K_A (V^* - |V_{DQ}|) \end{cases}$$

1-axis SG

$$\begin{cases} \frac{d\delta}{dt} &= \omega_s \Delta\omega \\ M \frac{\Delta\omega}{dt} &= -D \Delta\omega + P^* - P \\ T'_{do} \frac{E_q}{dt} &= -E_q - (X_d - X'_d) I_d + V_{fd} \\ T_E \frac{dV_{fd}}{dt} &= -(K_E + S_E(V_{fd})) V_{fd} + V_R \\ T_F \frac{dR_f}{dt} &= -R_f + \frac{K_F}{T_F} V_{fd} \\ T_A \frac{dV_R}{dt} &= -V_R + K_A R_f - \frac{K_A K_F}{T_F} V_{fd} + K_A (V^* - |V_{DQ}|) \end{cases}$$

Classical SG

$$\begin{cases} \frac{d\delta}{dt} &= \omega_s \Delta\omega \\ M \frac{\Delta\omega}{dt} &= -D \Delta\omega + P^* - P \\ T_E \frac{dV_{fd}}{dt} &= -(K_E + S_E(V_{fd})) V_{fd} + V_R \\ T_F \frac{dR_f}{dt} &= -R_f + \frac{K_F}{T_F} V_{fd} \\ T_A \frac{dV_R}{dt} &= -V_R + K_A R_f - \frac{K_A K_F}{T_F} V_{fd} + K_A (V^* - |V_{DQ}|) \end{cases}$$

3.4 Mathematical Modeling of Cascaded PI Controller

As described in Chapter 2, the original implementations of the main VSM topologies did not consider cascaded loops. Instead, they simply generated the reference current and voltage for controlling the converter via $P - \omega$ (realized as the SG swing equation) and $Q - V$ droop laws.

However, in addition to the active and reactive power control, modifications in the original topologies described in Chapter 2 considered an additional cascaded inner loop to realize the zero-error tracking of the converter output current or voltage reference, thus ensuring accurate execution of the outer loop control, which regulates the active and reactive powers [36]. In the CVSM topology, a double-loop PI voltage and current control is used to further improve the control dynamics, and better dampen the resonances caused by the converter output filters [27].

In Figure 3.12, we simplify the block diagram of Figure 2.9, assuming that the feed-forward terms are always included ($k_{ff_i} = k_{ff_v} = 1$) and removing the active damping terms. Moreover, we change the variable names to those to be used in this thesis.

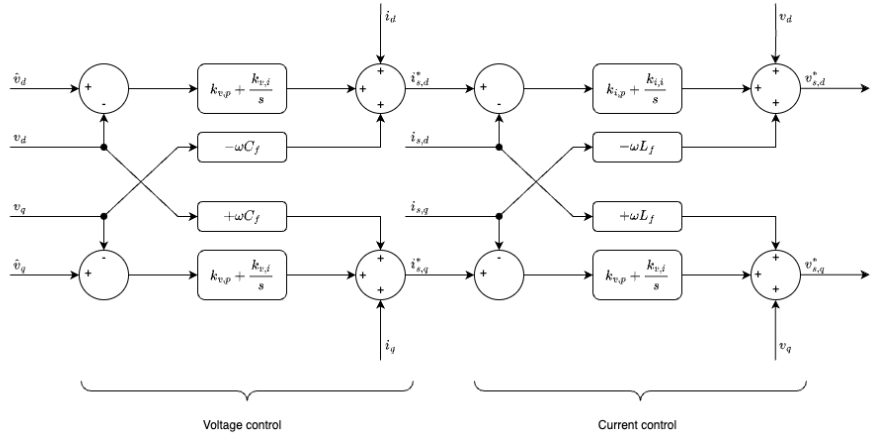


Figure 3.12: Block diagram of the cascaded PI controller.

It is important to note that the feed-forward terms are used for decoupling the dynamics of the converter and the AC power grid, improving the disturbance rejection capability and avoiding the converter's start up transients [33]. The block diagram of Figure 3.12 can be mathematically described by [27, 30]:

$$\begin{cases} \dot{x}_{v,dq} = \hat{v}_{dq} - v_{dq} \\ i_{s,dq}^* = i_{dq} + \omega C_f \mathcal{J}_2 v_{dq} + k_{v,p} \mathcal{I}_2 (\hat{v}_{dq} - v_{dq}) + k_{v,i} \mathcal{I}_2 x_{v,dq} \end{cases} \quad (3.7)$$

$$\begin{cases} \dot{x}_{i,dq} = i_{s,dq}^* - i_{s,dq} \\ v_{s,dq}^* = v_{dq} + \omega L_f \mathcal{J}_2 i_{s,dq} + k_{i,p} \mathcal{I}_2 (i_{s,dq}^* - i_{s,dq}) + k_{i,i} \mathcal{I}_2 x_{i,dq} \end{cases} \quad (3.8)$$

where \mathcal{I}_2 is the identity matrix of order 2 and $x_{v,dq}$ and $x_{i,dq}$ are the integrators' internal state. The reference voltage $v_{s,dq}^*$ is then used for generating the modulation signal for controlling the converter such that $v_{s,dq} = v_{s,dq}^*$.

3.5 Calculation of Equilibrium Point

$$\left\{ \begin{array}{l} L_f \frac{di_{s,dq}}{dt} = -\omega L_f \mathcal{J}_2 i_{s,dq} + m_{dq} \frac{v_{dc}}{2} - v_{dq} \\ C_f \frac{dv_{dq}}{dt} = -\omega C_f \mathcal{J}_2 v_{dq} + i_{s,dq} - i_{dq} \\ L_g \frac{di_{dq}}{dt} = -\omega L_g \mathcal{J}_2 i_{dq} + v_{dq} - V_{dq} \\ \frac{d\delta}{dt} = \omega_s \Delta \omega \\ M \frac{\Delta \omega}{dt} = -D \Delta \omega + P^* - P \\ T'_{do} \frac{E_q}{dt} = -E_q - (X_d - X'_d) I_d + V_{fd} \\ T'_{qo} \frac{E_d}{dt} = -E_d + (X_q - X'_q) I_q \\ T_E \frac{dV_{fd}}{dt} = -(K_E + S_E(V_{fd})) V_{fd} + V_R \\ T_F \frac{dR_f}{dt} = -R_f + \frac{K_F}{T_F} V_{fd} \\ T_A \frac{dV_R}{dt} = -V_R + K_A R_f - \frac{K_A K_F}{T_F} V_{fd} + K_A (V^* - |V_{DQ}|) \\ \dot{x}_{v,dq} = \hat{v}_{dq} - v_{dq} \\ \dot{x}_{i,dq} = i_{s,dq}^* - i_{s,dq} \end{array} \right. \quad (3.9)$$

Appendices

Appendix A

Synchronous Generators

Synchronous generators form the backbone of contemporary power generation, converting the mechanical energy sourced from fossil fuel combustion or natural resources like water streams into electrical energy. Their operation at a constant speed synchronized with the AC power frequency has made them a staple in the field since the late 19th century.

This chapter delves into the enduring role of synchronous generators, focusing on their operational intricacies and control strategies. Over the years, various control methods, including Automatic Voltage Regulation (AVR), Power System Stabilization (PSS), and Automatic Generation Control (AGC), have been developed to ensure the stable performance of these machines.

The objective of this chapter is to elucidate key concepts and models associated with synchronous generators, providing a foundation for understanding their behavior. For a more detailed explanation in the modeling of synchronous generators, please refer to [28],[32] and [37].

A.1 Modeling of Synchronous Generators

A.1.1 General Structure of Synchronous Generators

A synchronous generator is mainly composed by a stator, in which three-phase windings are placed 120° apart in space, and a rotor, in which a field winding and three damper windings are placed. The field winding is connected to a DC current source, and the currents in the damper windings flow such that their magnetic fluxes are along the d - and q -axes, perpendicular to the rotor's axis. The following figure is a diagram of a three-phase synchronous generator.

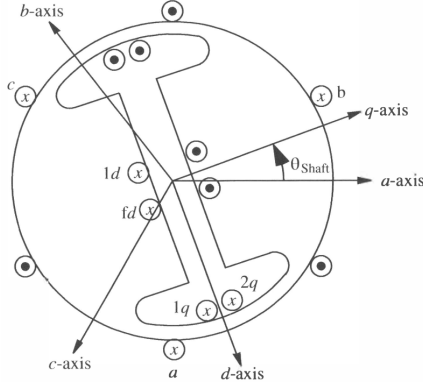


Figure A.1: Schematic diagram of a three-phase synchronous generator [28].

The assumptions made in the mathematical modeling of the synchronous generators are:

1. Stator windings are distributed sinusoidally along the air gap;
2. Stator slots do not cause any variation in the rotor inductances;
3. Magnetic hysteresis is negligible;
4. Magnetic circuit is considered linear.
5. The rotor has a single pair of poles.

Assumptions 1 to 3 are reasonable since the manufacturing process of synchronous machines is very precise. Assumption 4 is made for simplification, but in more complete analysis the nonlinearities of the magnetic circuit should be taken into account [29]. By applying the fundamental Kirchhoff's, Faraday's and Newton's laws, the following relationships can be derived.

$$\left\{ \begin{array}{l} \frac{d\delta}{dt} = \omega_s \Delta\omega \\ M \frac{d\omega}{dt} = -D \Delta\omega + P_m - P_e \\ v_a = -i_a r_s + \frac{d\lambda_a}{dt} \\ v_b = -i_b r_s + \frac{d\lambda_b}{dt} \\ v_c = -i_c r_s + \frac{d\lambda_c}{dt} \\ v_{fd} = i_{fd} r_{fd} + \frac{d\lambda_{fd}}{dt} \\ v_{1d} = i_{1d} r_{1d} + \frac{d\lambda_{1d}}{dt} \\ v_{1q} = i_{1q} r_{1q} + \frac{d\lambda_{1q}}{dt} \\ v_{2q} = i_{2q} r_{2q} + \frac{d\lambda_{2q}}{dt} \end{array} \right. \quad (\text{A.1})$$

where v_i are the instantaneous phase to neutral voltage, i_i are the currents, r_i are the resistances and λ_i are the flux linkages in each phase i . Moreover, M is the inertia coefficient, D is the damping coefficient, P_m is the mechanical torque applied to the shaft, P_e is the electrical torque, δ is the rotor angle θ_{shaft} relative to a rotating frame that rotates with constant speed equal to the synchronous speed ω_s , and $\Delta\omega = \omega - \omega_s$, where ω is the rotor's rotational speed.

A.1.2 Linear Magnetic Circuit

Considering the special case in which the magnetic circuit of the synchronous generator is linear in relation to the currents, the flux linkages can be expressed in the following matrix form [37]:

$$\begin{bmatrix} \lambda_a \\ \lambda_b \\ \lambda_c \end{bmatrix} = - \begin{bmatrix} l_{aa} & l_{ab} & l_{ac} \\ l_{ab} & l_{bb} & l_{bc} \\ l_{ac} & l_{bc} & l_{cc} \end{bmatrix} \begin{bmatrix} i_a \\ i_b \\ i_c \end{bmatrix} + \begin{bmatrix} l_{afd} & l_{a1d} & l_{a1q} & l_{a2q} \\ l_{afd} & l_{b1d} & l_{b1q} & l_{b2q} \\ l_{afd} & l_{b1d} & l_{c1q} & l_{c2q} \end{bmatrix} \begin{bmatrix} i_{fd} \\ i_{1d} \\ i_{1q} \\ i_{2q} \end{bmatrix} \quad (\text{A.2})$$

$$\begin{bmatrix} \lambda_{fd} \\ \lambda_{1d} \\ \lambda_{1q} \\ \lambda_{2q} \end{bmatrix} = - \begin{bmatrix} l_{fda} & l_{fdb} & l_{fdc} \\ l_{1da} & l_{1db} & l_{1dc} \\ l_{1qa} & l_{1qb} & l_{1qc} \\ l_{2qa} & l_{2qb} & l_{2qc} \end{bmatrix} \begin{bmatrix} i_a \\ i_b \\ i_c \end{bmatrix} + \begin{bmatrix} l_{fdfd} & l_{fd1d} & 0 & 0 \\ l_{1dfd} & l_{1d1d} & 0 & 0 \\ 0 & 0 & l_{1q1q} & l_{1q2q} \\ 0 & 0 & l_{2q1q} & l_{2q2q} \end{bmatrix} \begin{bmatrix} i_{fd} \\ i_{1d} \\ i_{1q} \\ i_{2q} \end{bmatrix} \quad (\text{A.3})$$

Note that the mutual inductances between the d - and q -axes are zero, since they are perpendicular between each other. In normal operation, the angle between the windings in the rotor and in the stator are constantly changing, thus the inductances vary according to the angle θ_{shaft} .

From definition, inductance is equal to the ratio of magnetic flux to current, magnetic flux is the product of permeance and magnetomotive force, and magnetomotive force is the product of the current around the turns and the number of turns of a coil[38]. In other words:

$$\begin{aligned} l &= \frac{\lambda}{i} \\ \lambda &= N\phi, \\ \phi &= FP, \\ F &= Ni \end{aligned}$$

where ϕ is magnetic flux, N is the number of turns of the coil, P is the permeance and F is the magnetomotive force. In order to understand how the inductances vary according to θ_{shaft} , let us analyze the magnetomotive force (mmf) in the a -winding of Figure A.1. Let $F_a = N_a i_a$ be the mmf in the a -winding, it can be split in the d - and q -axes as follows:

$$\begin{aligned} F_{ad} &= F_a \sin(\theta_{\text{shaft}}) \\ F_{aq} &= F_a \cos(\theta_{\text{shaft}}) \end{aligned} \quad (\text{A.4})$$

Let P_d and P_q be the permeances along the d - and q -axes, respectively, the total flux is therefore:

$$\begin{aligned} \phi_{aa} &= F_{ad}P_d \sin(\theta_{\text{shaft}}) + F_{aq}P_q \cos(\theta_{\text{shaft}}) \\ &= F_a P_d \sin^2(\theta_{\text{shaft}}) + F_a P_q \cos^2(\theta_{\text{shaft}}) \\ &= N_a i_a \left(\frac{P_d(1 - \cos(2\theta_{\text{shaft}}))}{2} + \frac{P_q(1 + \cos(2\theta_{\text{shaft}}))}{2} \right) \\ &= N_a i_a \left(\frac{P_d + P_q}{2} - \frac{P_d - P_q}{2} \cos(2\theta_{\text{shaft}}) \right) \end{aligned} \quad (\text{A.5})$$

Thus, the self-inductance l_{aa} can be written as:

$$l_{aa} = l_{aa0} - l_{aap} \cos(2\theta_{shaft})$$

where:

$$l_{aa0} = N_a^2 \left(\frac{P_d + P_q}{2} \right) \quad \text{and} \quad l_{aap} = N_a^2 \left(\frac{P_d - P_q}{2} \right)$$

Repeating the same procedure for the other windings, the matrices in Equations A.2 and A.3 become:

$$\begin{aligned} L_{ss} &= \begin{bmatrix} l_{aa} & l_{ab} & l_{ac} \\ l_{ab} & l_{bb} & l_{bc} \\ l_{ac} & l_{bc} & l_{cc} \end{bmatrix} \\ &= \begin{bmatrix} l_{aa0} - l_{aap} \cos(2\theta_{shaft}) & -\frac{1}{2}l_{aa0} - l_{aap} \cos(2\theta_{shaft} - \frac{2\pi}{3}) \\ -\frac{1}{2}l_{aa0} - l_{aap} \cos(2\theta_{shaft} - \frac{2\pi}{3}) & l_{aa0} - l_{aap} \cos(2\theta_{shaft} + \frac{2\pi}{3}) \\ -\frac{1}{2}l_{aa0} - l_{aap} \cos(2\theta_{shaft} + \frac{2\pi}{3}) & -\frac{1}{2}l_{aa0} - l_{aap} \cos(2\theta_{shaft}) \end{bmatrix} \\ &\quad \begin{bmatrix} -\frac{1}{2}l_{aa0} - l_{aap} \cos(2\theta_{shaft} + \frac{2\pi}{3}) \\ -\frac{1}{2}l_{aa0} - l_{aap} \cos(2\theta_{shaft}) \\ l_{aa0} - l_{aap} \cos(2\theta_{shaft} - \frac{2\pi}{3}) \end{bmatrix} \\ L_{sr} &= \begin{bmatrix} l_{afd} & l_{a1d} & l_{a1q} & l_{a2q} \\ l_{afd} & l_{b1d} & l_{b1q} & l_{b2q} \\ l_{afd} & l_{b1d} & l_{c1q} & l_{c2q} \end{bmatrix} \\ &= \begin{bmatrix} l_{sfd} \sin(\theta_{shaft}) & l_{s1d} \sin(\theta_{shaft}) \\ l_{sfd} \sin(\theta_{shaft} - \frac{2\pi}{3}) & l_{s1d} \sin(\theta_{shaft} - \frac{2\pi}{3}) \\ l_{sfd} \sin(\theta_{shaft} + \frac{2\pi}{3}) & l_{s1d} \sin(\theta_{shaft} + \frac{2\pi}{3}) \\ l_{s1q} \cos(\theta_{shaft}) & l_{s2q} \cos(\theta_{shaft}) \\ l_{s1q} \cos(\theta_{shaft} - \frac{2\pi}{3}) & l_{s2q} \cos(\theta_{shaft} - \frac{2\pi}{3}) \\ l_{s1q} \cos(\theta_{shaft} + \frac{2\pi}{3}) & l_{s2q} \cos(\theta_{shaft} + \frac{2\pi}{3}) \end{bmatrix} \end{aligned}$$

where:

$$\begin{aligned} l_{afd} &= l_{bfd} = l_{cfid} = l_{sfd} \\ l_{a1d} &= l_{b1d} = l_{c1d} = l_{s1d} \\ l_{a1q} &= l_{b1q} = l_{c1q} = l_{s1q} \\ l_{a2q} &= l_{b2q} = l_{c2q} = l_{s2q} \end{aligned}$$

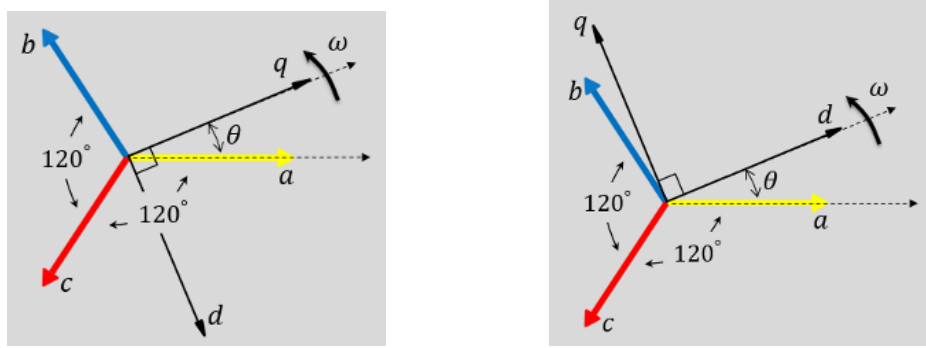
Since the above matrices vary with θ_{shaft} , it is convenient to make a coordinate transformation to a rotating reference system with same speed as θ_{shaft} so that the trigonometrical terms disappear. This coordinate transformation is referred to Park's transformation (or $dq0$ -transformation) and drastically reduces the complexity of the equations.

A.1.3 Park's Transformation ($dq0$ -transformation)

In power systems, the $dq0$ -transformation, also known as Park's transformation, consists in converting from the static abc frame to a rotating $dq0$ frame. The main objective of this transformation is to reduce a three-phase sinusoidal components into two-dimensional DC components, and therefore it results in

relatively simple dynamic models that can be controlled through classical PID controllers.

This transformation slightly differs from author to author depending on the choice of the leading and lagging components. For instance, in [28] the authors consider the a-axis and the q-axis initially aligned, while in [32] the authors consider the a-axis and the d-axis initially aligned.



(a) The a-axis and the q-axis are initially aligned.
(b) The a-axis and the d-axis are initially aligned.

Figure A.2: Different representations of $dq\theta$ frame.

In this thesis, the a-axis and the q-axis are chosen to be initially aligned. In this case, the Park transformation can be expressed by the following transformation matrix from abc frame to the rotating $dq0$ frame.

$$T_{dq0} = \frac{2}{3} \begin{bmatrix} \sin(\theta) & \sin(\theta - \frac{2\pi}{3}) & \sin(\theta + \frac{2\pi}{3}) \\ \cos(\theta) & \cos(\theta - \frac{2\pi}{3}) & \cos(\theta + \frac{2\pi}{3}) \\ \frac{1}{2} & \frac{1}{2} & \frac{1}{2} \end{bmatrix} \quad (\text{A.6})$$

The inverse transformation can be expressed by the following matrix.

$$T_{dq0}^{-1} = \begin{bmatrix} \sin(\theta) & \cos(\theta) & 1 \\ \sin(\theta - \frac{2\pi}{3}) & \cos(\theta - \frac{2\pi}{3}) & 1 \\ \sin(\theta + \frac{2\pi}{3}) & \cos(\theta + \frac{2\pi}{3}) & 1 \end{bmatrix} \quad (\text{A.7})$$

Applying this transformation to the stator voltages, i.e. the first three equations in Equation A.1:

$$\begin{aligned} \begin{bmatrix} v_d \\ v_q \\ v_0 \end{bmatrix} &= -T_{dq0} \begin{bmatrix} r_s & 0 & 0 \\ 0 & r_s & 0 \\ 0 & 0 & r_s \end{bmatrix} T_{dq0}^{-1} \begin{bmatrix} i_d \\ i_q \\ i_0 \end{bmatrix} + T_{dq0} \frac{d}{dt} \left(T_{dq0}^{-1} \begin{bmatrix} \lambda_d \\ \lambda_q \\ \lambda_0 \end{bmatrix} \right) \\ &= - \begin{bmatrix} r_s & 0 & 0 \\ 0 & r_s & 0 \\ 0 & 0 & r_s \end{bmatrix} \begin{bmatrix} i_d \\ i_q \\ i_0 \end{bmatrix} + T_{dq0} \frac{dT_{dq0}^{-1}}{dt} \left(\begin{bmatrix} \lambda_d \\ \lambda_q \\ \lambda_0 \end{bmatrix} \right) + \frac{d}{dt} \left(\begin{bmatrix} \lambda_d \\ \lambda_q \\ \lambda_0 \end{bmatrix} \right) \\ &= - \begin{bmatrix} r_s & 0 & 0 \\ 0 & r_s & 0 \\ 0 & 0 & r_s \end{bmatrix} \begin{bmatrix} i_d \\ i_q \\ i_0 \end{bmatrix} + \begin{bmatrix} 0 & -\omega & 0 \\ \omega & 0 & 0 \\ 0 & 0 & 0 \end{bmatrix} \begin{bmatrix} \lambda_d \\ \lambda_q \\ \lambda_0 \end{bmatrix} + \frac{d}{dt} \left(\begin{bmatrix} \lambda_d \\ \lambda_q \\ \lambda_0 \end{bmatrix} \right) \end{aligned}$$

Therefore, the Equation A.1 in the $dq0$ coordinates has the forms:

$$\left\{ \begin{array}{l} \frac{d\delta}{dt} = \omega_s \Delta\omega \\ M \frac{\Delta\omega}{dt} = -D \Delta\omega + P_m - P_e \\ v_d = -r_s i_d - \omega \lambda_q + \frac{d\lambda_d}{dt} \\ v_q = -r_s i_q + \omega \lambda_d + \frac{d\lambda_q}{dt} \\ v_0 = -r_s i_0 + \frac{d\lambda_0}{dt} \\ v_{fd} = r_{fd} i_{fd} + \frac{d\lambda_{fd}}{dt} \\ v_{1d} = r_{1d} i_{1d} + \frac{d\lambda_{1d}}{dt} \\ v_{1q} = r_{1q} i_{1q} + \frac{d\lambda_{1q}}{dt} \\ v_{2q} = r_{2q} i_{2q} + \frac{d\lambda_{2q}}{dt} \end{array} \right. \quad (\text{A.8})$$

Moreover, in order to calculate the stator fluxes in the $dq0$ coordinates, let us apply the transformations A.6 and A.7 to Equations A.2 and A.3. For the explicit calculation, please refer to [32].

$$\begin{aligned} \lambda_d &= -(l_{md} + l_{ls}) i_d + l_{sfd} i_{fd} + l_{s1d} i_{1d} \\ \lambda_q &= -(l_{mq} + l_{ls}) i_d + l_{s1q} i_{fd} + l_{s2q} i_{1d} \\ \lambda_0 &= -l_{ls} i_0 \\ \lambda_{fd} &= -\frac{3}{2} l_{sfd} i_d + l_{fd} i_{fd} + l_{fd1d} i_{1d} \\ \lambda_{1d} &= -\frac{3}{2} l_{s1d} i_d + l_{fd1d} i_{fd} + l_{1d1d} i_{1d} \\ \lambda_{1q} &= -\frac{3}{2} l_{s1q} i_q + l_{1q1q} i_{1q} + l_{1q2q} i_{2q} \\ \lambda_{2q} &= -\frac{3}{2} l_{s2q} i_q + l_{1q2q} i_{1q} + l_{2q2q} i_{2q} \end{aligned} \quad (\text{A.9})$$

where l_{md} , l_{mq} and l_{ls} are, respectively, the mutual inductance in the d - and q -axes and the leakage inductance.

A.1.4 Per-Unit System

In power system studies, it is customary to scale all quantities using the per-unit system. Typically, voltage and power are selected based on the equipment ratings, and base values such as current and impedance are derived from these. When studying a system, a convenient round number, such as 100 MVA, is often chosen as the base power, and the base voltage is usually set to the nominal rated value of the system. The key advantages of employing a per-unit system include:

- **Ease of comparison:** the per-unit system eliminates differences in power and voltage drops across a circuit, allowing for the comparison of losses and performance among different equipment based on their impedances in per units.
- **Simplification of circuits with transformers:** in power systems with transformers, converting a transformer into its equivalent circuit on either the primary or secondary side is necessary. However, using per-unit systems makes the impedances referred to either side of a transformer identical, eliminating the need to calculate impedances on both sides.

- **Elimination of multiple voltage levels:** in power systems with multiple transformers, the per-unit system reduces all voltage levels to a single level, simplifying calculations by referencing all impedances to this level.
- **Elimination of $\sqrt{3}$ in three-phase circuits:** Per-unit systems eliminate the need for the $\sqrt{3}$ factor in three-phase systems, avoiding errors and simplifying calculations that involve per-phase and line-to-line conversions.

Due to the composition of multiple coils in its stator and rotor, a synchronous generator can be treated as multiple transformers, each with different voltage levels. Therefore, the use of a per-unit system is highly beneficial for analyzing synchronous generators, ensuring that rotor and stator quantities are referred to the same base.

In the subsequent subsections, Equations A.8 and A.9 are reformulated in the per-unit system, giving rise to the Park's model of a synchronous generator, also known as the detailed model. Subject to certain assumptions, this detailed model will be further reduced into the 2-axis, 1-axis, and classical models of a synchronous generator. For a detailed explanation of the reformulation of Equations A.8 and A.9 in the per-unit system, please refer to [28] and [37].

A.1.5 Park's Model (Detailed Model)

The Park's model, also known as the detailed model, corresponds to Equations A.8 and A.9 reformulated in the per-unit system. It represents a 9th-order system comprising 2 mechanical equations describing rotor motion and 7 electromechanical equations describing the three stator windings and four rotor windings (one field winding, and one damper winding on the d -axis, and two damper windings on the q -axis).

$$\left\{ \begin{array}{l} \frac{d\delta}{dt} = \omega_s \Delta\omega \\ M \frac{\Delta\omega}{dt} = -D \Delta\omega + P_m - P_e \\ \frac{1}{\omega_s} \frac{d\psi_d}{dt} = R_s I_d + \frac{\omega}{\omega_s} \psi_q + V_d \\ \frac{1}{\omega_s} \frac{d\psi_q}{dt} = R_s I_q - \frac{\omega}{\omega_s} \psi_d + V_q \\ \frac{1}{\omega_s} \frac{d\psi_0}{dt} = R_s I_0 + V_0 \\ T'_{do} \frac{dE_q}{dt} = -E_q - (X_d - X'_d) \left(I_d - \frac{(X'_d - X''_d)}{(X'_d - X_{ls})^2} (\psi_{1d} + (X'_d - X_{ls}) I_d - E_q) + E_{fd} \right) \\ T''_{do} \frac{d\psi_{1d}}{dt} = -\psi_{1d} + E_q - (X'_d - X_{ls}) I_d \\ T'_{qo} \frac{dE_d}{dt} = -E_d - (X_q - X'_q) \left(I_q - \frac{(X'_q - X''_q)}{(X'_q - X_{ls})^2} (\psi_{2q} + (X'_q - X_{ls}) I_q + E_d) \right) \\ T''_{qo} \frac{d\psi_{2q}}{dt} = -\psi_{2q} - E_d - (X'_q - X_{ls}) I_q \\ \psi_d = -X''_d I_d + \frac{(X''_d - X_{ls})}{(X'_d - X_{ls})} E_q + \frac{(X'_d - X''_d)}{(X'_d - X_{ls})} \psi_{1d} \\ \psi_q = -X''_q I_q - \frac{(X''_q - X_{ls})}{(X'_q - X_{ls})} E_d + \frac{(X'_q - X''_q)}{(X'_q - X_{ls})} \psi_{2q} \\ \psi_0 = -X_{ls} I_0 \end{array} \right. \quad (A.10)$$

A.1.6 2-axis Model (Subtransient Model)

The Park's model can be reduced to a 4th-order system, also known as the 2-axis model (or subtransient model), by eliminating the stator/network transients and assuming that the short-circuit time constants T_{do}'' and T_{qo}'' are sufficiently small [28].

First, the stator/network transients can be eliminated by assuming that ω_s is large enough such that $\frac{1}{\omega_s} \approx 0$. Then, the stator/network fluxes in Equation A.10 become.

$$\begin{cases} 0 & = R_s I_d + \frac{\omega}{\omega_s} \psi_q + V_d \\ 0 & = R_s I_q - \frac{\omega}{\omega_s} \psi_d + V_q \\ 0 & = R_s I_0 + V_0 \\ \psi_d & = -X_d'' I_d + \frac{(X_d'' - X_{ls})}{(X_d' - X_{ls})} E_q + \frac{(X_d' - X_d'')}{(X_d' - X_{ls})} \psi_{1d} \\ \psi_q & = -X_q'' I_q - \frac{(X_q'' - X_{ls})}{(X_q' - X_{ls})} E_d + \frac{(X_q' - X_q'')}{(X_q' - X_{ls})} \psi_{2q} \\ \psi_0 & = -X_{ls} I_0 \end{cases}$$

The solution of the above equations of ψ_0 and I_0 is trivial, and ψ_d and ψ_q can be eliminated, leaving only the following two equations to be solved for I_d and I_q .

$$\begin{cases} 0 & = R_s I_d - X_q'' I_q - \frac{(X_q'' - X_{ls})}{(X_q' - X_{ls})} E_d + \frac{(X_q' - X_q'')}{(X_q' - X_{ls})} \psi_{2q} + V_d \\ 0 & = R_s I_q - X_d'' I_d - \frac{(X_d'' - X_{ls})}{(X_d' - X_{ls})} E_q - \frac{(X_d' - X_d'')}{(X_d' - X_{ls})} \psi_{1d} + V_q \end{cases} \quad (\text{A.11})$$

Moreover, assuming that the short-circuit time constants T_{do}'' and T_{qo}'' are sufficiently small, the damping winding dynamic equations in Equation A.10 become:

$$\begin{cases} 0 & = -\psi_{1d} + E_q - (X_d' - X_{ls}) I_d \\ 0 & = -\psi_{2q} - E_d - (X_q' - X_{ls}) I_q \end{cases}$$

Replacing ψ_{1d} and ψ_{2q} in Equation A.11:

$$\begin{cases} 0 & = R_s I_d - X_q' I_q - E_d + V_d \\ 0 & = R_s I_q + X_d' I_d - E_q + V_q \end{cases}$$

Finally, the Park's model is reduced to the two-axis model, also known as subtransient model, and it is expressed by the following set of dynamical equations.

$$\begin{cases} \frac{d\delta}{dt} & = \omega_s \Delta\omega \\ M \frac{d\omega}{dt} & = -D \Delta\omega + P_m - P_e \\ T_{do}' \frac{E_q}{dt} & = -E_q - (X_d - X_d') I_d + E_{fd} \\ T_{qo}' \frac{E_d}{dt} & = -E_d + (X_q - X_q') I_q \\ 0 & = R_s I_d - X_q' I_q - E_d + V_d \\ 0 & = R_s I_q + X_d' I_d - E_q + V_q \end{cases} \quad (\text{A.12})$$

A.1.7 1-axis Model (Flux-Decay Model)

The 2-axis model still considers the dynamics of the damper winding $1q$ illustrated in Figure A.1. Similarly to the approximation made for eliminating the damper windings $1d$ and $2q$ in the previous subsection, if T'_{qo} is sufficiently small, the dynamic equation of the damper winding $1q$ becomes:

$$0 = -E_d + (X_q - X'_q)I_q$$

Replacing E_d in the algebraic equations for I_d and I_q , the model described by Equation A.12 becomes:

$$\begin{cases} \frac{d\delta}{dt} &= \omega_s \Delta\omega \\ M \frac{\Delta\omega}{dt} &= -D \Delta\omega + P_m - P_e \\ T'_{do} \frac{E_q}{dt} &= -E_q - (X_d - X'_d)I_d + E_{fd} \\ 0 &= R_s I_d - X_q I_q + V_d \\ 0 &= R_s I_q + X'_d I_d - E_q + V_q \end{cases} \quad (\text{A.13})$$

which is often called the 1-axis (or flux-decay) synchronous machine model.

A.1.8 Classical Model

Finally, the classical model is a further simplification considering T'_{do} sufficiently small, and therefore the dynamic equation of the excitation winding can be ignored in the similar way as in the previous two subsections. In other words, the classical model only considers the mechanical dynamics of the synchronous generator, and can be described by the following set of equations.

$$\begin{cases} \frac{d\delta}{dt} &= \omega_s \Delta\omega \\ M \frac{\Delta\omega}{dt} &= -D \Delta\omega + P_m - P_e \\ 0 &= R_s I_d - X_q I_q + V_d \\ 0 &= R_s I_q + X_d I_d + V_q \end{cases} \quad (\text{A.14})$$

A.2 Modeling of Exciter and Automatic Voltage Regulator (AVR)

A.3 Modeling of Turbine/Governor

A.4 Power System Stabilizer (PSS)

A.5 Automatic Generation Control (AGC)

References

- [1] U. Nations, “The 17 sustainable development goals.” URL: <https://sdgs.un.org/goals>, 2015.
- [2] U. Nations, “Conference of the parties.” URL: <https://unfccc.int/process/bodies/supreme-bodies/conference-of-the-parties-cop>.
- [3] I. R. E. A. (IRENA), “World energy transitions outlook 2023: 1.5°C pathway,” 2023.
- [4] Y. Lin, J. H. Eto, B. B. Johnson, J. D. Flicker, R. H. Lasseter, H. N. Villegas Pico, G.-S. Seo, B. J. Pierre, and A. Ellis, “Research roadmap on grid-forming inverters,” tech. rep., National Renewable Energy Lab.(NREL), Golden, CO (United States), 11 2020.
- [5] M. S. Alam, F. S. Al-Ismail, A. Salem, and M. A. Abido, “High-level penetration of renewable energy sources into grid utility: Challenges and solutions,” *IEEE Access*, vol. 8, pp. 190277–190299, 2020.
- [6] P. Denholm, T. Mai, R. W. Kenyon, B. Kroposki, and M. O’Malley, “Inertia and the power grid: A guide without the spin,” tech. rep., National Renewable Energy Lab.(NREL), Golden, CO (United States), 2020.
- [7] M. Ndreko, S. Rüberg, and W. Winter, “Grid forming control for stable power systems with up to 100% inverter based generation: a paradigm scenario using the ieee 118-bus system,” in *Proceedings of the 17th International Wind Integration Workshop, Stockholm, Sweden*, pp. 16–18, 2018.
- [8] D. Pattabiraman, R. H. Lasseter., and T. M. Jahns, “Comparison of grid following and grid forming control for a high inverter penetration power system,” in *2018 IEEE Power & Energy Society General Meeting (PESGM)*, pp. 1–5, 2018.
- [9] E. Taylor, “Application of advanced grid-scale inverters in the nem,” tech. rep., Australian Energy Market Operator, 2021.
- [10] H.-P. Beck and R. Hesse, “Virtual synchronous machine,” in *2007 9th International Conference on Electrical Power Quality and Utilisation*, pp. 1–6, 2007.
- [11] C.-H. Zhang, Q.-C. Zhong, J.-S. Meng, X. Chen, Q. Huang, S.-h. Chen, and Z.-p. Lv, “An improved synchronverter model and its dynamic behaviour comparison with synchronous generator,” in *2nd IET Renewable Power Generation Conference (RPG 2013)*, pp. 1–4, 2013.

- [12] Q.-C. Zhong and G. Weiss, "Synchronverters: Inverters that mimic synchronous generators," *IEEE Transactions on Industrial Electronics*, vol. 58, no. 4, pp. 1259–1267, 2011.
- [13] J. Alipoor, Y. Miura, and T. Ise, "Power system stabilization using virtual synchronous generator with alternating moment of inertia," *IEEE Journal of Emerging and Selected Topics in Power Electronics*, vol. 3, no. 2, pp. 451–458, 2015.
- [14] M. Chen, D. Zhou, and F. Blaabjerg, "Modelling, implementation, and assessment of virtual synchronous generator in power systems," *Journal of Modern Power Systems and Clean Energy*, vol. 8, no. 3, pp. 399–411, 2020.
- [15] J. Driesen and K. Visscher, "Virtual synchronous generators," in *2008 IEEE Power and Energy Society General Meeting - Conversion and Delivery of Electrical Energy in the 21st Century*, pp. 1–3, 2008.
- [16] Y. Hirase, K. Abe, K. Sugimoto, and Y. Shindo, "A grid-connected inverter with virtual synchronous generator model of algebraic type," *Electrical Engineering in Japan*, vol. 184, no. 4, pp. 10–21, 2013.
- [17] K. Sakimoto, Y. Miura, and T. Ise, "Stabilization of a power system with a distributed generator by a virtual synchronous generator function," in *8th International Conference on Power Electronics - ECCE Asia*, pp. 1498–1505, 2011.
- [18] J. Liu, Y. Miura, H. Bevrani, and T. Ise, "Enhanced virtual synchronous generator control for parallel inverters in microgrids," *IEEE Transactions on Smart Grid*, vol. 8, no. 5, pp. 2268–2277, 2017.
- [19] Y. Chen, R. Hesse, D. Turschner, and H.-P. Beck, "Improving the grid power quality using virtual synchronous machines," in *2011 international conference on power engineering, energy and electrical drives*, pp. 1–6, IEEE, 2011.
- [20] Y. Chen, R. Hesse, D. Turschner, and H.-P. Beck, "Comparison of methods for implementing virtual synchronous machine on inverters," in *International conference on renewable energies and power quality*, vol. 1, 2012.
- [21] T. Shintai, Y. Miura, and T. Ise, "Reactive power control for load sharing with virtual synchronous generator control," in *Proceedings of The 7th International Power Electronics and Motion Control Conference*, vol. 2, pp. 846–853, 2012.
- [22] J. Liu, *Studies on Improving Dynamic Performance of Microgrids by Applying Virtual Synchronous Generator Control to Distributed Generators*. PhD thesis, Osaka University, 2016.
- [23] Q.-C. Zhong, P.-L. Nguyen, Z. Ma, and W. Sheng, "Self-synchronized synchronverters: Inverters without a dedicated synchronization unit," *IEEE Transactions on Power Electronics*, vol. 29, no. 2, pp. 617–630, 2014.

- [24] Z. Shuai, W. Huang, C. Shen, J. Ge, and Z. J. Shen, “Characteristics and restraining method of fast transient inrush fault currents in synchronverters,” *IEEE Transactions on Industrial Electronics*, vol. 64, no. 9, pp. 7487–7497, 2017.
- [25] S. D’Arco, J. A. Suul, and O. B. Fosso, “Control system tuning and stability analysis of virtual synchronous machines,” in *2013 IEEE Energy Conversion Congress and Exposition*, pp. 2664–2671, 2013.
- [26] S. D’Arco, J. A. Suul, and O. B. Fosso, “Small-signal modelling and parametric sensitivity of a virtual synchronous machine,” in *2014 Power Systems Computation Conference*, pp. 1–9, 2014.
- [27] S. D’Arco, J. A. Suul, and O. B. Fosso, “A virtual synchronous machine implementation for distributed control of power converters in smartgrids,” *Electric Power Systems Research*, vol. 122, pp. 180–197, 2015.
- [28] P. W. Sauer, M. A. Pai, and J. H. Chow, *Power system dynamics and stability: with synchrophasor measurement and power system toolbox*. John Wiley & Sons, 2017.
- [29] P. S. Kundur and O. P. Malik, *Power System Stability and Control*. McGraw Hill, 2022.
- [30] A. Tayyebi, D. Groß, A. Anta, F. Kupzog, and F. Dörfler, “Frequency stability of synchronous machines and grid-forming power converters,” *IEEE Journal of Emerging and Selected Topics in Power Electronics*, vol. 8, no. 2, pp. 1004–1018, 2020.
- [31] Y. Ma, W. Cao, L. Yang, F. Wang, and L. M. Tolbert, “Virtual synchronous generator control of full converter wind turbines with short-term energy storage,” *IEEE Transactions on Industrial Electronics*, vol. 64, no. 11, pp. 8821–8831, 2017.
- [32] P. C. Krause, O. Wasenczuk, S. D. Sudhoff, and S. Pekarek, *Analysis of electric machinery and drive systems*, vol. 2. Wiley Online Library, 2002.
- [33] A. Yazdani and R. Iravani, *Voltage-sourced converters in power systems: modeling, control, and applications*. John Wiley & Sons, 2010.
- [34] C.-H. Zhang, Q.-C. Zhong, J.-S. Meng, X. Chen, Q. Huang, S.-h. Chen, and Z.-p. Lv, “An improved synchronverter model and its dynamic behaviour comparison with synchronous generator,” in *2nd IET Renewable Power Generation Conference (RPG 2013)*, pp. 1–4, 2013.
- [35] V. Knazkins, *Stability of power systems with large amounts of distributed generation*. PhD thesis, Elektrotekniska system, 2004.
- [36] F. Blaabjerg, *Control of Power Electronic Converters and Systems: Volume 2*, vol. 2. Academic Press, 2018.
- [37] S. Sivasubramani, “Synchronous machine modeling.” URL: https://www.iitp.ac.in/~siva/2022/ee549/Synchronous_Machine_Modelling.pdf, 2022.

- [38] E. M. Purcell and D. J. Morin, *Electricity and Magnetism*. Cambridge University Press, 2013.